

Search for New Physics in All-hadronic Events with AlphaT in 8 TeV Data at CERN

by

Yossof Eshaq

Submitted in Partial Fulfillment of the

Requirements for the Degree

Doctor of Philosophy

Supervised by Professor Aran Garcia-Bellido

Department of Physics & Astronomy

Arts, Sciences and Engineering

School of Arts and Sciences

University of Rochester

Rochester, New York

2014

Acknowledgements

I would like to thank my parents Hugo and Virginia for their unconditional love and support. They have poured everything they have into me and made me what I am. This Thesis is dedicated to them.

I thank my colleagues in the UC physics department, past and present. I thank my supervisor Alan J. Schwartz for his continual support throughout my tenure as a graduate student, and for bringing me to Belle during my first year at UC. His knowledge, patience, understanding, and dedication to both his work and his students has been and will continue to be a source of inspiration for me. Words cannot describe how grateful I am for everything he has done. I also thank Kay Kinoshita, Alexander Somov, Alexey Drutskoy, Seema Bahinipati and Kazi Sayeed for their support, encouragement, and patience (especially at the beginning with all of my questions).

I am incredibly grateful to the many hundreds of people that makeup the Belle collaboration and the KEKB accelerator team. I spent the majority of my time living in Japan and have developed wonderful relationships, both professionally and socially, with many amazing people. It is impossible for me to list all of the people that I want to thank here. Please know that you are all in my heart. I would like to thank Jasna Dragic for dragging me to my first HH meeting and guiding me through my first presentation at Belle. Her constant support and encouragement proved instrumental to my growth. I also thank Mikihiro Nakao, Tom Browder, Paoti Chang, Yoshihide Sakai and all of the regular attendees of the HH, DVPC, BAM and BGM meetings for providing critical assessments and suggestions, and for always keeping pace and monitoring my progress. Without their guidance and the structure they provided me I would surely have been lost in the wilderness. I only hope that I can pass on all of the knowledge they have bestowed upon me to future generations of students. It has been an honor to work with you all.

Contents

Abstract	2
Acknowledgments	4
Contents	5
List of Figures	7
List of Tables	13
1 Theoretical motivation	16
1.1 The Standard Model	16
1.2 Supersymmetry	16
2 LHC and CMS	17
3 Data sets and Monte Carlo samples	18
3.1 Data sets	18
3.2 MC samples for signal and SM backgrounds	18
3.3 Corrections to cross sections for SM samples	19
4 Event Selection	23
4.1 Data	24
4.2 Event quality	24
4.3 Physics objects	25
4.3.1 Jets	25
4.3.2 Muons	26
4.3.3 Photons	26

4.3.4	Electrons	27
4.3.5	Missing transverse energy	27
4.3.6	Single isolated tracks	28
4.4	Triggers	29
4.4.1	Hadronic signal region and control samples	29
4.5	Object vetoes	32
4.6	Hadronic pre-selection	32
4.7	Definition of α_T	34
4.8	Final selections	37
5	Background estimation for processes with genuine E_T	39
5.1	Overview of the method	40
5.2	Definition of the control samples	41
5.2.1	Muon and photon triggers	42
5.2.2	The μ + jets control sample	44
5.2.3	The γ + jets control sample	45
6	Closure tests and systematic uncertainties on transfer factors	46
6.1	Closure tests	46
6.2	Systematic uncertainties from closure tests	49
7	Signal models and efficiencies	52
7.1	Introduction	52
7.2	Efficiency times acceptance	53
8	Systematic uncertainties on signal efficiency times acceptance	55
8.1	Introduction	55

8.2	PDF uncertainties	55
8.3	Jet energy scale	56
8.4	Initial state radiation	56
8.5	b-tag scale factor corrections	57
8.6	Total systematic uncertainties	57
9	Results	61
9.1	Standard Model	61
A	Maximum likelihood parameter values	69
B	SM-only yield tables	76
C	Efficiencies and systematic uncertainties for simplified models	79
C.1	T2cc	79
C.2	T2tt	84

List of Figures

1	Generator-level H_T^{parton} distributions and measured weights	22
2	H_T distribution after basic preselection, for 35 pb ⁻¹ of data collected at 7 TeV as well as for all standard model backgrounds and two SUSY signal samples, from [?]]. This figure is for illustrative purposes only, as these specific SUSY models are not under study in this analysis	23
3	Cumulative efficiency turn-on curves for the H_T - α_T cross triggers (as summarized in Table 7) that record events for the three lowest H_T bins for events satisfying $2 \leq n_{\text{jet}} \leq 3$ (left) and $n_{\text{jet}} \geq 4$ (right).	31
4	α_T distribution for 11.7 fb ⁻¹ of data collected at 8 TeV as well as for all standard model backgrounds and one example SUSY signal sample, from [?]]. This figure is for illustrative purposes only, as this analysis relies on data control samples to estimate contribution from SM process with genuine E_T	35
5	Data–MC comparison of the α_T distribution after following the application of the hadronic pre-selection criteria for events satisfying $n_{\text{jet}} > 2$ and $n_b > 0$ in histograms with (a) coarse and (b) fine binning).	36
6	Data–MC comparisons of key variables for the hadronic signal region, following the application of the full signal region selection criteria and the requirements $H_T > 375$ GeV and $\alpha_T > 0.55$: (a) n_{jet} , (b) n_b , (c) H_T , and (d) E_T distributions for an inclusive selection on n_{jet} and n_b , and (e,f) H_T for the two event categories ($2 \leq n_{\text{jet}} \leq 3$, $n_b = 0$) and ($n_{\text{jet}} \geq 4$, $n_b = 1$).	38
7	(left) Muon trigger efficiency as a function of number of primary vertices for muon $p_T > 25$ GeV and $ \eta < 2.1$., (right) number of primary vertices in muon control sample.	42

8	Cumulative efficiency turn-on curves for the HLT_Photon150 trigger as a function of photon p_T for events satisfying $2 \leq n_{\text{jet}} \leq 3$ (left) and $n_{\text{jet}} \geq 4$ (right).	43
9	Sets of closure tests (open symbols) overlaid on top of the systematic uncertainty used for each of the H_T region (shaded bands) and for the two different jet multiplicity bins: (a) $2 \leq n_{\text{jet}} \leq 3$ and (b) $n_{\text{jet}} \geq 4$	51
10	Hadronic selection efficiency times acceptance for T2cc for the relevant event categories defined by n_{jet} and n_b . Note the different z-axis scales.	53
11	Hadronic selection efficiency times acceptance for the T2tt for the relevant event categories defined by n_{jet} and n_b . Note the different z-axis scales.	54
12	The total systematic uncertainty in the signal efficiency times acceptance for all relevant event categories for the T2cc interpretation.	58
13	The total systematic uncertainty in the signal efficiency times acceptance for all relevant event categories for the T2tt interpretation.	59
14	Pulls and p-values. See text for details	62
15	Comparison of the H_T -binned observed data yields and SM expectations when requiring $2 \leq n_{\text{jet}} \leq 3$ and $n_b = 0$ for the (a-b) hadronic, (c) $\mu + \text{jets}$, (d) $\mu\mu + \text{jets}$ and (e) $\gamma + \text{jets}$ samples, as determined by a simultaneous fit to all data samples under the SM-only hypothesis. The observed event yields in data (black dots) and the expectations and their uncertainties (dark blue solid line with light blue bands), as determined by the simultaneous fit, are shown. For illustrative purposes only, the signal expectations (pink dashed line) for the model T2cc with $m_{\tilde{q}} = 250$ GeV and $m_{\text{LSP}} = 240$ GeV are stacked on top of the SM expectations.	63

- 16 Comparison of the H_T -binned observed data yields and SM expectations when requiring $2 \leq n_{\text{jet}} \leq 3$ and $n_b = 1$ for the (a-b) hadronic, (c) $\mu + \text{jets}$, (d) $\mu\mu + \text{jets}$ and (e) $\gamma + \text{jets}$ samples, as determined by a simultaneous fit to all data samples under the SM-only hypothesis. The observed event yields in data (black dots) and the expectations and their uncertainties (dark blue solid line with light blue bands), as determined by the simultaneous fit, are shown. For illustrative purposes only, the signal expectations (pink dashed line) for the model T2cc with $m_{\tilde{q}} = 250 \text{ GeV}$ and $m_{\text{LSP}} = 170 \text{ GeV}$ are stacked on top of the SM expectations. 64
- 17 Comparison of the H_T -binned observed data yields and SM expectations when requiring $2 \leq n_{\text{jet}} \leq 3$ and $n_b = 2$ for the (a-b) hadronic and $\mu + \text{jets}$ samples, as determined by a simultaneous fit to both the hadronic and $\mu + \text{jets}$ data samples under the SM-only hypothesis. The observed event yields in data (black dots) and the expectations and their uncertainties (dark blue solid line with light blue bands), as determined by the simultaneous fit, are shown. 65
- 18 Comparison of the H_T -binned observed data yields and SM expectations when requiring $n_{\text{jet}} \geq 4$ and $n_b = 0$ for the (a-b) hadronic, (c) $\mu + \text{jets}$, (d) $\mu\mu + \text{jets}$ and (e) $\gamma + \text{jets}$ samples, as determined by a simultaneous fit to all data samples under the SM-only hypothesis. The observed event yields in data (black dots) and the expectations and their uncertainties (dark blue solid line with light blue bands), as determined by the simultaneous fit, are shown. For illustrative purposes only, the signal expectations (pink dashed line) for the model T2cc with $m_{\tilde{q}} = 250 \text{ GeV}$ and $m_{\text{LSP}} = 170 \text{ GeV}$ are stacked on top of the SM expectations. 66

- 19 Comparison of the H_T -binned observed data yields and SM expectations when requiring $n_{\text{jet}} \geq 4$ and $n_b = 1$ for the (a-b) hadronic, (c) $\mu + \text{jets}$, (d) $\mu\mu + \text{jets}$ and (e) $\gamma + \text{jets}$ samples, as determined by a simultaneous fit to all data samples under the SM-only hypothesis. The observed event yields in data (black dots) and the expectations and their uncertainties (dark blue solid line with light blue bands), as determined by the simultaneous fit, are shown. For illustrative purposes only, the signal expectations (pink dashed line) for the model T2cc with $m_{\tilde{q}} = 250$ GeV and $m_{\text{LSP}} = 170$ GeV are stacked on top of the SM expectations. 67
- 20 Comparison of the H_T -binned observed data yields and SM expectations when requiring $n_{\text{jet}} \geq 4$ and $n_b = 2$ for the (a-b) hadronic and $\mu + \text{jets}$ samples, as determined by a simultaneous fit to both the hadronic and $\mu + \text{jets}$ data samples under the SM-only hypothesis. The observed event yields in data (black dots) and the expectations and their uncertainties (dark blue solid line with light blue bands), as determined by the simultaneous fit, are shown. 68
- 21 Ratio of efficiency times acceptance for the (middle) central value, (top) $+1\sigma$ value, (bottom) -1σ value of the envelope calculation relative to the nominal PDF set used to produce the T2cc sample. 79
- 22 The fractional change in signal efficiency due to systematically (Left) increasing and (Middle) decreasing all jet energies, and (Right) the resulting (symmetric) systematic uncertainties due to JES uncertainties for T2cc. 80
- 23 The fractional change in signal efficiency due to systematically (Left) increasing and (Middle) decreasing event weights according to ISR uncertainties, and (Right) the resulting (symmetric) systematic uncertainties due to ISR uncertainties for T2cc. 81

24	The fractional change in signal efficiency due to systematically (Left) increasing and (Middle) decreasing all b-tag efficiencies according to the scale factor uncertainties, and (Right) the resulting (symmetric) systematic uncertainties due to b-tag scale factor uncertainties for T2cc.	82
25	The total systematic uncertainty in the signal efficiency times acceptance for all relevant event categories for the T2cc interpretation.	83
26	Ratio of efficiency times acceptance for the (middle) central value, (top) $+1\sigma$ value, (bottom) -1σ value of the envelope calculation relative to the nominal PDF set used to produce the T2tt sample.	84
27	The fractional change in signal efficiency due to systematically (Left) increasing and (Middle) decreasing all jet energies, and (Right) the resulting (symmetric) systematic uncertainties due to JES uncertainties for T2tt.	85
28	The fractional change in signal efficiency due to systematically (Left) increasing and (Middle) decreasing event weights according to ISR uncertainties, and (Right) the resulting (symmetric) systematic uncertainties due to ISR uncertainties for T2tt.	86
29	The fractional change in signal efficiency due to systematically (Left) increasing and (Middle) decreasing all b-tag efficiencies according to the scale factor uncertainties, and (Right) the resulting (symmetric) systematic uncertainties due to b-tag scale factor uncertainties for T2tt.	87

List of Tables

1	Datasets.	18
2	MC samples for Standard Model processes.	19
3	Corrections determined from a data sideband for the $W + \text{jets}$ and $t\bar{t}$ samples. “Corrected yield” reflects the observed data yield minus the contamination as given by MC.	21
4	Muon identification (Tight working point).	26
5	Photon identification (Tight working point).	27
6	Electron identification (Loose working point).	27
7	List of signal triggers and their efficiencies (%), as measured in data. The trigger efficiency is $\sim 100\%$ for all bins above $H_T > 675 \text{ GeV}$	30
8	Jet E_T thresholds per H_T bin.	33
9	Summary of control samples used to predict the SM background for each event category.	41
10	A summary of the results obtained from fits of zeroth order polynomials (i.e. a constant) to four sets of closure tests performed in the $2 \leq n_{\text{jet}} \leq 3$ bin.	48
11	A summary of the results obtained from fits of zeroth order polynomials (i.e. a constant) to three sets of closure tests performed in the $n_{\text{jet}} \geq 4$ bin. [†] Further explanation of this fit can be found in the text.	48
12	A summary of the results obtained from fits of zeroth order polynomials (i.e. a constant) to four sets of closure tests ($2 \leq n_{\text{jet}} \leq 3 \rightarrow n_{\text{jet}} \geq 4$) that probe the accuracy of the MC modeling of the n_{jet} distribution observed in data, using the three data control samples.	49
13	A summary of the magnitude of the systematic uncertainties (%) obtain from closure tests, according to n_{jet} and H_T region.	49

14	A summary of the magnitude of the total systematic uncertainties (%) assigned to the transfer factors, according to n_{jet} and H_T region.	50
15	A summary of the simplified models considered for interpretation. The event categories considered for each model are listed.	52
16	Sparticle system p_T dependent corrections and systematic weight variations.	57
17	Representative ranges for each contribution to the total systematic uncertainty in the signal efficiency times acceptance for each relevant event category for the T2cc interpretation.	59
18	Representative ranges for each contribution to the total systematic uncertainty in the signal efficiency times acceptance for each relevant event category for the T2tt interpretation.	60
19	Summary of hadronic yields from fit.	62
20	SM-only maximum-likelihood parameter values (0b le3j).	70
21	SM-only maximum-likelihood parameter values (1b le3j).	71
22	SM-only maximum-likelihood parameter values (2b le3j).	72
23	SM-only maximum-likelihood parameter values (0b ge4j).	73
24	SM-only maximum-likelihood parameter values (1b ge4j).	74
25	SM-only maximum-likelihood parameter values (2b ge4j).	75
26	0b le3j	76
27	0b ge4j	76
28	1b le3j	77
29	1b ge4j	77
30	2b le3j	77
31	2b ge4j	78

pagenumberingarabic

1 Theoretical motivation

1.1 The Standard Model

SM,Higgs

Particle physics concerns itself with the study of particles and fields. Our current knowledge of their characteristics and interactions are formalized in the quantum field theory called the Standard Model. It through three symmetries: The color charge symmetry of Quantum Chromo Dynamics (QCD) represented in $SU(3)$, the flavor symmetry of Quantum Flavor Dynamics (QFD) represented in $SU(2)$ and the electric charge symmetry of Quantum Electro Dynamics represented in $U(1)$. Together, $SU(3) \times SU(2) \times U(1)$ represent the field theory.

1.2 Supersymmetry

Susy

2 LHC and CMS

LHC, CMS

3 Data sets and Monte Carlo samples

3.1 Data sets

The data analyzed consist of the full run of 2012.

The following datasets are used to populate the hadronic signal and control samples. They correspond to the full data run of 2012 and an integrated luminosity of $19.45 \pm 0.8 \text{ fb}^{-1}$. The official JSON from the 22nd Jan 2013 is used to filter only certified luminosity sections with the run range 190456–208686.

Table 1: Datasets.

Dataset	Luminosity (fb^{-1})
Hadronic	19.45
Muon	19.72
Photon	19.63

3.2 MC samples for signal and SM backgrounds

The SM background Monte Carlo samples for physics at 8 TeV are taken from the Summer12 simulation production run with CMSSW_5_3_X with the PU_S10 scenario. The effective luminosity of each MC sample is normalized to the integrated luminosity of the corresponding dataset, as listed in Table 2. The signal MADGRAPH Monte Carlo samples, listed in Table ??, are taken from a FastSim simulation production based on CMSSW_5_2_X. All MC samples are reweighted on an event-by-event basis such that the distribution of pile-up (PU) interactions matches that observed in data. This is done using the recommended recipe and the PU JSON of 13th December 2012.

Table 2: MC samples for Standard Model processes.

Sample	HT (GeV)	Cross section (pb)	Corrected Cross section (pb)
$W \rightarrow l\nu$	Inclusive	37509.0	34133.2
$W \rightarrow l\nu$	150 - 200	253.8	234.53
$W \rightarrow l\nu$	200 - 250	116.5	103.94
$W \rightarrow l\nu$	250 - 300	57.6	51.34
$W \rightarrow l\nu$	300 - 400	48.4	42.41
$W \rightarrow l\nu$	400 - ∞	30.8	26.36
$Z \rightarrow \nu\bar{\nu}$	50 - 100	452.8	405.21
$Z \rightarrow \nu\bar{\nu}$	100 - 200	190.4	173.76
$Z \rightarrow \nu\bar{\nu}$	200 - 400	45.1	42.41
$Z \rightarrow \nu\bar{\nu}$	400 - ∞	6.26	5.81
$t\bar{t}$	Inclusive	234.0	271.44
$Z/\gamma^* \rightarrow l^+l^- (m_{ll} > 50)$	Inclusive	3503.7	3258.45
$Z/\gamma^* \rightarrow l^+l^- (10 < m_{ll} < 50)$	Inclusive	13124.1	12205.4
$Z/\gamma^* \rightarrow l^+l^-$	200 - 400	24.3	22.24
$Z/\gamma^* \rightarrow l^+l^-$	400 - ∞	3.36	3.11
γ + jets	200 - 400	1140.8	1060.9
γ + jets	400 - ∞	124.7	115.97
WW	Inclusive	57.1	57.1
WZ	Inclusive	12.6	12.6
ZZ	Inclusive	8.26	8.26
t (t-channel)	Inclusive	56.4	56.4
\bar{t} (t-channel)	Inclusive	30.7	30.7
t (s-channel)	Inclusive	3.79	3.79
\bar{t} (s-channel)	Inclusive	1.76	1.76
t (tW-channel)	Inclusive	11.1	11.1
\bar{t} (tW-channel)	Inclusive	11.1	11.1

3.3 Corrections to cross sections for SM samples

A simulated event is weighted by the total number of events in the MC sample, the theoretical cross section, and total luminosity of the data being studied. The MC Pog provides next-to-next-to leading order (NNLO) theoretical cross section for un-filtered (inclusive) SM samples [?]. In an attempt to provide higher statistics in tails of distribution analyses often cut on (ie H_T^{parton} , N^{parton} , \hat{p}_T), MC samples are provided binned in these variables. Only the leading-order (LO) cross sections are provided [?] but in general, the k -factors required to go from LO to NNLO cross sections are determined using corresponding inclusive samples and applied to each binned sample.

Studies conducted by other analyses [?] revealed that some LO cross sections calculated for MC samples binned according to H_T^{parton} are inaccurate to a level as large as 10%, leading to

non-physical discontinuities in the H_T^{parton} distribution constructed from the binned samples of a given process. Furthermore, due to an error in production, the $W \rightarrow l\nu$ H_T binned samples exhibit H_T -dependent biases. The following paragraphs describes a procedure to measure corrections to the discontinuities and biases of the $W \rightarrow l\nu$ H_T^{parton} binned samples as a function of H_T . Other analyses created similar procedures to correct the $Z \rightarrow \mu\mu$ H_T^{parton} binned samples, this analysis uses those measured corrections as k-factors.

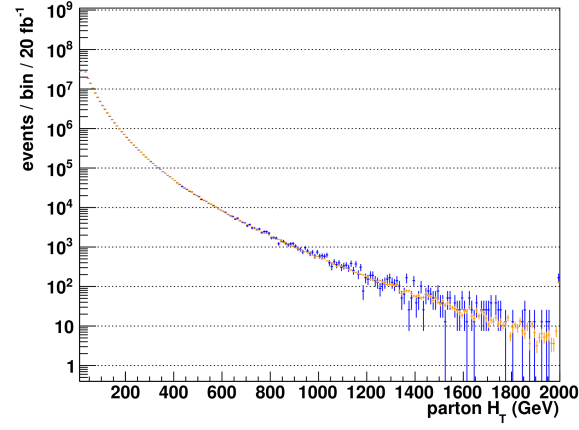
As a first step, we wish to reweigh the cross sections of the H_T^{parton} binned samples such that their H_T^{parton} distributions match that of the inclusive sample's. Due to the inclusive sample's limited statistics in the tails of H_T distribution, we instead use the N^{parton} binned's H_T^{parton} distribution which is verified to agree well with the inclusive sample figure 1 (a). Additionally, to smooth statistical fluctuations, both distributions are fitted using a double exponential of the form $\exp(a + b * x + c * x^{1.05})$ for $H_T > 500$ GeV figure 1 (b). The ratio of the distributions figure 1(c) is applied as H_T^{parton} dependent event weight.

In the high- H_T and high- E_T corner of kinematic phase space of this analysis (and other SUSY analyses) the overall normalization of MC samples do not agree well with data. Therefore a data sideband in H_T is used to determine sample-specific corrections that are appropriate for the H_T - E_T phase space covered by this analysis. This correction is determined for the $W \rightarrow l\nu$ and $t\bar{t}$ samples by imposing requirements on the number of muons, jets, and b-tagged jets, to obtain samples rich in W + jets, and $t\bar{t}$ events. A sideband in H_T is used to determine both the yields in data and MC expectations. The sideband is defined by the region $200 < H_T < 225$ GeV and uses the jet p_T thresholds (73, 73, 37 GeV) to maintain comparable jet multiplicities, kinematics. and background admixtures as observed for the higher H_T bins. Trigger efficiency and b-tag scale factor corrections are determined and applied to the MC samples. The purity of the samples are $> 80\%$ and any contamination is taken into account. The correction is determined by taking the ratio of the data yield over the MC expectation in the sideband. Table 3 summarizes the selection and corrections

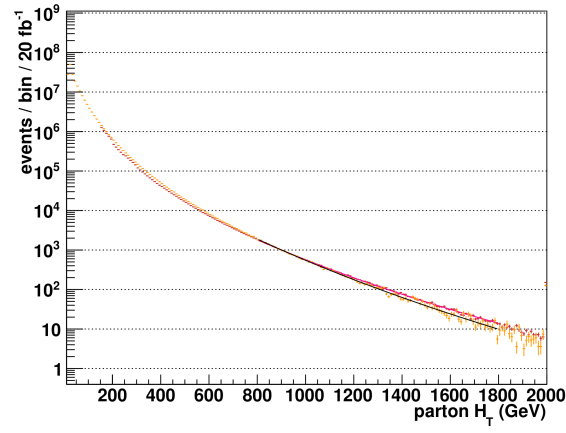
for the different samples.

Table 3: Corrections determined from a data sideband for the $W + \text{jets}$ and $t\bar{t}$ samples. “Corrected yield” reflects the observed data yield minus the contamination as given by MC.

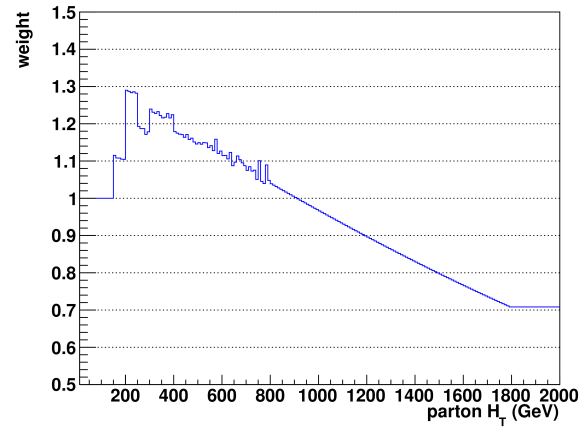
Process	Selection	Purity	Corrected yield	MC expectation	Correction Factor
$W + \text{jets}$	$\mu + \text{jets}, 2 \leq n_{\text{jet}} \leq 3, n_b = 0$	0.90	15682	18013.1 ± 85.9	0.87 ± 0.01
$t\bar{t}$	$\mu + \text{jets}, n_{\text{jet}} \geq 2, n_b \geq 2$	0.83	752	736.7 ± 11.5	1.02 ± 0.05



(a) Parton H_T distribution for the $W \rightarrow l\nu$ inclusive sample (blue) and $W \rightarrow l\nu N^{\text{parton}}$ binned sample (orange.)



(b) Fitted Parton H_T distribution for the $W \rightarrow l\nu H_T^{\text{parton}}$ sample (purple) and $W \rightarrow l\nu N^{\text{parton}}$ binned sample (orange.)



(c) Event weight determined from ratio of figure 1 (b)

Figure 1: Generator-level H_T^{parton} distributions and measured weights

4 Event Selection

As discussed in section 1.2, all-hadronic SUSY signatures consist of events with no isolated and detectable objects apart from energetic jets. One can quantify the total visible energy in these type of events with the quantity, H_T , the scalar sum of the transverse energy of the jets in the event. The challenges due to large backgrounds in a search for an excess in all-hadronic events becomes evident when comparing observed data events overlaid with simulated events from SM processes as a function of H_T , figure 2.

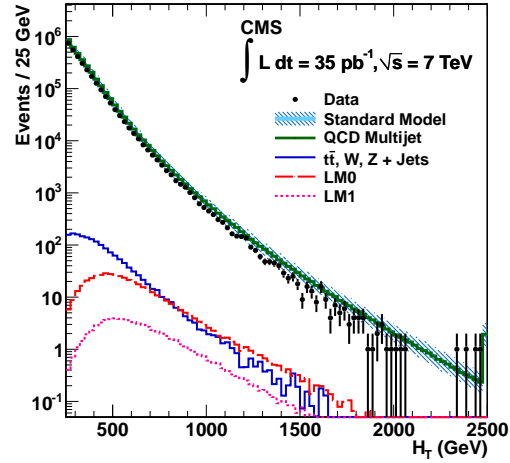


Figure 2: H_T distribution after basic preselection, for 35 pb^{-1} of data collected at 7 TeV as well as for all standard model backgrounds and two SUSY signal samples, from [?]. This figure is for illustrative purposes only, as these specific SUSY models are not under study in this analysis

The dominant background are azimuthally-balanced (i.e. back-to-back in the azimuthal angle ϕ) multi-jet events, stemming from QCD processes. This search reduces this background to negligible levels in the hadronic search region by employing the α_T variable further discussed in section 4.7. Furthermore, by construction, α_T also reduces backgrounds from mis-measured back-to-back jets. In the absence of the multi-jet QCD events, the remaining significant backgrounds

are SM process with genuine E_T . The expected yield of these backgrounds are measured using two control samples. The following sections describe the identification of objects used in the hadronic and control samples, while the detailed description of the background and control samples are left for chapter 5.

4.1 Data

The data analyzed was recorded by CMS in 2012 between April 5th and Dec. 5th and totals $19.47 \pm 0.5 \text{ fb}^{-1}$. The collected data is certified on a run-by-run basis, where initial automatic certification requires the LHC beams to be declared stable and all CMS subdetectors ON. Further monitoring of the data was done in real-time by experts of each subdetector through analysis of histograms updated and filled each luminosity section. Final certification was done offline, and luminosity sections passing all criteria were listed in a Golden JSON file to be used by all analyses.

4.2 Event quality

Each event is subjected to a series of commonly used filters in CMS to ensure good data quality. Minimal requirements are that at least one primary vertex is identified and 25% of the reconstructed tracks to be of good quality. Additionally, various event cleaning filters prescribed by the MET group [?] are applied. These filters reject events containing known problems, such as: muons with inconsistent energy or muons created by beam-gas interactions, spurious noise spikes in the calorimeter, tracking failures, and calibration lasers polluting overlapping with physics collisions.

4.3 Physics objects

The following subsections describe the definitions of the physics objects used in this analysis.

4.3.1 Jets

Jets are reconstructed by combining information from multiple sub-detectors using the Particle-Flow (PF) algorithm [?] and clustered by the anti- k_T algorithm [?] with a size parameter of 0.5. Three levels of jet energy corrections are applied; level 1 corrects for overlapping pp collisions (pile-up [? ?]) in the jet, level 2 and 3 correct the jet energy response to be η and p_T independent. Further residual corrections are applied on data which correct for small remaining discrepancies in the modelling of the response. The acceptance of “fake” and poorly reconstructed jets is suppressed by selecting jets that pass jet identification at the Loose working point [?]. This requires that the jet is comprised of more than one particle and that those particles cannot all be neutral hadrons or all neutral particle deposits in the ECAL. Additionally if the jet is reconstructed beyond the tracker’s instrumentation, i.e. $|\eta| < 2.4$, the jet is required to have more than one charged constituent, of which not all of them deposit their energy in the ECAL. Only jets reconstructed within the barrel and endcap of the calorimeters, i.e. $|\eta| < 3.0$, and with transverse momentum $p_T > 50 \text{ GeV}$ are considered in the analysis. Jets originating from bottom quarks (b-jets) are identified through vertices that are displaced with respect to the primary interaction [?]. The algorithm used to tag b-jets is the Combined Secondary Vertex tagger, using the “Medium” working point, which is achieved by requiring a cut of >0.679 on the algorithm discriminator variable and results in a gluon/light-quark quark mis-tag rate of 1% (where “light” means u , d and s quarks) and an efficiency in the range 60 – 70% depending on the jet p_T .

4.3.2 Muons

Muons are identified according to the Tight working point definition ($\sim 95\%$ efficiency) of the muon identification algorithm [?]. The algorithm works to reject cosmic muons or muons from decays in flight for consideration in the analysis. A PF-based “combined relative” isolation [?] is determined within a cone size $\Delta R < 0.4$, and corrections are applied to remove the effects of pileup. Table 4 summarizes the identification and isolation requirements.

Table 4: Muon identification (Tight working point).

Global Muon	True
PFMuon	True
χ^2 fit	< 10
Muon chamber hits	> 0
Muon station hits	> 1
Transverse impact d_{xy}	< 0.2 mm
Longitudinal dist d_z	< 0.5 mm
Pixel hits	> 0
Track layer hits	> 5
PF Isolation ($\Delta\beta$ corrected)	< 0.12

4.3.3 Photons

Selected photons must satisfy the Tight working point definition ($\sim 70\%$ efficiency) of the simple cut-based photon identification algorithm [?]. The ECAL energy deposits from electrons are checked to have come from a converted photon. The ratio of energy deposits between HCAL and ECAL for a solid cone of size $\Delta R = 0.15$ is required to less than 5%. A maximum is set on the width of the clusted energy deposit, $\sigma_{i\eta i\eta}$, as decay photons from neutral pions typically have larger widths. Pile-up corrected isolation is determined within a cone of size $\Delta R < 0.3$ using the PF-based isolation algorithm [?]. Table 5 summarises the identification and isolation requirements.

Table 5: Photon identification (Tight working point).

Categories	Barrel	EndCap
Conversion safe electron veto	Yes	Yes
Single Tower H/E	0.05	0.05
$\sigma_{i\eta i\eta}$	0.11	0.31
PF charged hadron isolation	0.70	0.50
PF neutral hadron isolation	$0.4 + 0.04 \times p_T^\gamma$	$1.5 + 0.04 \times p_T^\gamma$
PF photon isolation	$0.5 + 0.005 \times p_T^\gamma$	$1.0 + 0.005 \times p_T^\gamma$

4.3.4 Electrons

Electrons are identified according to the “Veto” working point definition ($\sim 95\%$ efficiency) of the cut-based Egamma identification algorithm [?]. PF-based isolation [?] is determined within a cone size $\Delta R < 0.3$ and corrections are applied to remove the effects of pileup. Table 6 summarises the identification and isolation requirements.

Table 6: Electron identification (Loose working point).

Categories	Barrel	EndCap
$\Delta\eta_{In}$	0.007	0.009
$\Delta\phi_{In}$	0.15	0.10
$\sigma_{i\eta i\eta}$	0.01	0.03
H/E	0.12	0.10
d0 (vtx)	0.02	0.02
dZ (vtx)	0.2	0.20
$ (1/E_{\text{ECAL}} - 1/p_{\text{trk}}) $	0.05	0.05
PF relative isolation	0.15	0.15
Vertex fit probability	10^{-6}	10^{-6}
Missing hits	1	1

4.3.5 Missing transverse energy

Missing transverse energy, E_T , is defined as the scalar sum of the transverse momenta of all reconstructed objects. The analysis uses the particle-flow MET algorithm [?] with jet energy corrections

applied. The E_T variable is only used in the following two cases: to define of the tranverse mass variable, M_T , which is in turn used as part of the selection criteria that define the $\mu + \text{jets}$ control sample, described in section 5.2; to define a cleaning filter applied after the α_T requirement, as described in section 4.8.

4.3.6 Single isolated tracks

A single isolated track (SIT) [?] can be used to identify W bosons through their leptonic decays. A single isolated track is identified if a charged PF object has at least a p_T of 10 GeV, is near the primary vertex ($\Delta z(\text{track}, \text{PV}) < 0.05 \text{ cm}$) and has a relative track isolation of < 0.1 . This object can be used to help suppress the “lost lepton” background from W and $t\bar{t}$, as described in section 4.5.

4.4 Triggers

4.4.1 Hadronic signal region and control samples

Only events passing one or more HLT triggers based on online quantities are recorded to be analyzed. In any analysis, it is generally not expected that all recorded events reconstructed offline, pass the online trigger as detector conditions, energy corrections, and object-based quantities differ offline. In this analysis, cross-triggers at the HLT based on quantities H_T and α_T (labeled as HTxxx_AlphaT0pyy) are used with various thresholds to record candidate events for the hadronic search region. In order to keep the cross-trigger's computational time low, the online quantities are constructed using calorimeter based jets (calo jets), and the use of particle-flow jets in this analysis is expected to introduce inefficiencies. Each H_T bin is seeded by a single trigger chosen based on the efficiency of the trigger in that H_T bin. The α_T thresholds of the HTxxx_AlphaT0pyy triggers were tuned according to the threshold on the H_T leg in order to fully suppress QCD multijet events [?] and simultaneously satisfying other criteria, such as maintaining acceptable trigger rates.

The HTxxx_AlphaT0pyy trigger efficiencies are measured with a reference (i.e., unbiased) event sample recorded by an unprescaled, loosely-isolated, eta-restricted single muon trigger, HLT_IsoMu24_eta2p1, within the SingleMu dataset. A sample of events containing at least one isolated muon with $p_T > 25 \text{ GeV}$ and $|\eta| < 2.1$ is used (similar to the $\mu + \text{jets}$ control sample defined in section 5.2). A cut of $\Delta R > 0.5$ is placed between all muons and jets in each event, and only jets are considered in the calculation of H_T , H_T , and α_T , i.e. the muon is ignored.

Table 7 summarizes the measured efficiencies for the HTxxx_AlphaT0pyy triggers in the relevant H_T bins. The trigger efficiencies are measured for both n_{jet} multiplicity bins. seeds for which thresholds were raised to a relatively high level in order to maintain trigger rates in the high-pileup conditions towards the end of Run 1. The efficiencies are slightly lower in the higher jet multiplicity category due to a larger number of jets summing to the same H_T , resulting in softer jets.

Table 7: List of signal triggers and their efficiencies (%), as measured in data. The trigger efficiency is $\sim 100\%$ for all bins above $H_T > 675$ GeV.

Offline H_T region (GeV)	Offline α_T threshold	L1 seed (L1_?) (highest thresholds)	Trigger (HLT_?)	Efficiency (%)	
				$2 \leq n_{\text{jet}} \leq 3$	$n_{\text{jet}} \geq 4$
$375 < H_T < 475$	0.55	DoubleJetC64 OR HTT175	HT300_AlphaT0p53	$94.2^{+0.5}_{-0.6}$	$90.5^{+1.2}_{-1.3}$
$475 < H_T < 575$	0.55	DoubleJetC64 OR HTT175	HT350_AlphaT0p52	$96.2^{+0.8}_{-0.9}$	$94.6^{+1.2}_{-1.4}$
$575 < H_T < 675$	0.55	DoubleJetC64 OR HTT175	HT400_AlphaT0p51	$95.4^{+1.4}_{-1.8}$	$98.7^{+0.7}_{-1.12}$
$H_T > 675$	0.55	DoubleJetC64 OR HTT175	HT400_AlphaT0p51	$100^{+0.0}_{-2.0}$	$100^{+0.0}_{-2.0}$

Figure 3 shows the efficiency curves for the HTxxx_AlphaT0pyy triggers in the three lowest H_T bins, for the $2 \leq n_{\text{jet}} \leq 3$ and $n_{\text{jet}} \geq 4$ categories.

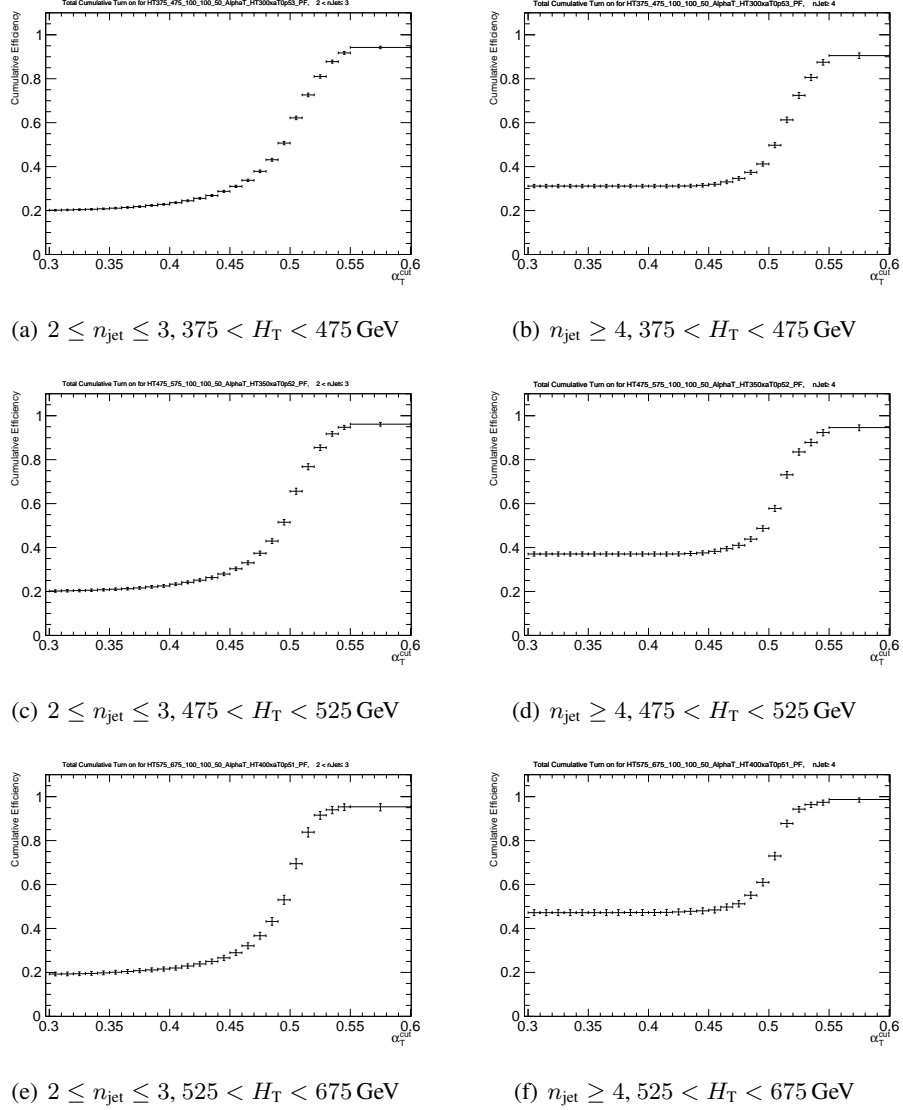


Figure 3: Cumulative efficiency turn-on curves for the H_T - α_T cross triggers (as summarized in Table 7) that record events for the three lowest H_T bins for events satisfying $2 \leq n_{\text{jet}} \leq 3$ (left) and $n_{\text{jet}} \geq 4$ (right).

4.5 Object vetoes

The background in this search can be separated into two types: reducible and irreducible. The latter refers to backgrounds that have the same final state as the signal and therefore any cut imposed to reduce the background would also reduce the signal. The process $Z \rightarrow \nu\bar{\nu} + \text{jets}$ is the only irreducible background in this search. All other backgrounds are reducible, meaning that if no information in the event is lost and all cuts were fully efficient, the background could be eliminated without loss of signal. To suppress $W + \text{jets}$ and $t\bar{t}$ events this analysis uses object vetoes to reject events where a W boson decays to a neutrino and a lepton. Events containing an isolated electron [?] with $p_T > 20 \text{ GeV}$ and $|\eta| < 2.5$ or an isolated muon [?] with $p_T > 10 \text{ GeV}$ and $|\eta| < 2.5$ are vetoed. In order to keep this search all-hadronic and not overlap with other analyses in CMS [? ?], events with isolated photons [?] with $p_T > 25 \text{ GeV}$ and $|\eta| < 2.5$ are also rejected. Events with a single isolated track 4.3.6 and no object associated with it can indicate that a lepton was “lost” (i.e. either fallen out of acceptance or poorly reconstructed), hence such events are vetoed. Detector and selection inefficiencies restrict the complete elimination of reducible backgrounds, as such, the method to estimate expected SM yields in the hadronic search region is described in section 5.

4.6 Hadronic pre-selection

Events are categorized into two jet multiplicities: $2 \leq n_{\text{jet}} \leq 3$ and $n_{\text{jet}} \geq 4$. Each event in these categories is further binned by the number of jets identified as originating from b quarks (n_b). Events having three or more b -tagged jets are not considered in the analysis. Significant hadronic activity in the events is ensured by requiring $H_T > 375 \text{ GeV}$. As described in section 4.4.1, events are further binned in 100 GeV bins starting from $H_T = 375 \text{ GeV}$ and ending with an open-ended bin $H_T > 1075 \text{ GeV}$. The two highest- p_T jets are subject to a higher threshold, $p_T > 100 \text{ GeV}$ and the highest- E_T jet is subjected to a tighter η acceptance requirement ($|\eta| < 2.5$). The variables H_T and H_T are computed from the number of jets, n_{jet} , that satisfy the p_T requirements listed in

Table 8.

Table 8: Jet E_T thresholds per H_T bin.

H_T bin	>375
Lead jet	100.0
Second jet	100.0
All other jets	50.0

4.7 Definition of α_T

Multi-jet events stemming from QCD contribute overwhelmingly to all-hadronic events recorded by the detector. Generally, these QCD events have no significant imbalance in transverse energy and can be reduced with a requirement for high- E_T . Yet, this approach is difficult, as the calculation of E_T is sensitive to detector effects and conditions, and additionally, in the high- E_T phase space systematic uncertainties become difficult to control. The variable, α_T , introduced in 2008 by Randall and Tucker-Smith [?] effectively suppresses multi-jet events with no significant met without relying on the measurement of E_T . By construction it also introduces robustness against mismeasurements of transverse energies in multi-jet systems. In the simplest case of a two-jet system, α_T is defined as

$$\alpha_T = \frac{E_T^{j2}}{M_T}, \quad (1)$$

where E_T^{j2} is the transverse energy of the less energetic jet and M_T is the transverse mass of the dijet system, defined as

$$M_T = \sqrt{\left(\sum_{i=1}^2 E_T^{ji}\right)^2 - \left(\sum_{i=1}^2 p_x^{ji}\right)^2 - \left(\sum_{i=1}^2 p_y^{ji}\right)^2} = \sqrt{H_T^2 + (H_\perp)^2}. \quad (2)$$

where the three terms, E_T^{ji} , p_x^{ji} , and p_y^{ji} are, respectively, the transverse energy and x or y components of the transverse momentum of jet j_i . By definition, the sum over the first term is H_T and the sums over the other two terms define H_\perp . In well measured QCD dijet events, transverse momentum conservation requires the p_T of the two jets to be of equal magnitude and back-to-back in the plane transverse to the beam. The value of α_T for these type of events can be best seen after transforming equation 2 into CMS coordinates:

$$\alpha_T = \frac{E_T^{j2}}{\sqrt{2E_T^{j1} E_T^{j2} (1 - \cos(\Delta\phi))}}. \quad (3)$$

Well balanced back-to-back jets have α_T values of 0.5. For the case of an imbalance in the measured transverse energies of back-to-back jets α_T is reduced to values smaller than 0.5, this gives the variable its robustness with respect to jet energy mismeasurements. In the case where the two jets are not back-to-back in the transverse plane but rather the dijet system balances genuine E_T , for example in leptonically decaying W boson recoiling off a system of jets, the values of α_T can exceed 0.5. Figure 4 shows the α_T distribution in two jet multiplicity bins for events passing an HT trigger and basic pre-selection requirements. Multi-jet events from QCD drop to negligible levels above $\alpha_T > 0.55$ while events with genuine E_T continue to populate bins in excess of $\alpha_T > 0.55$.

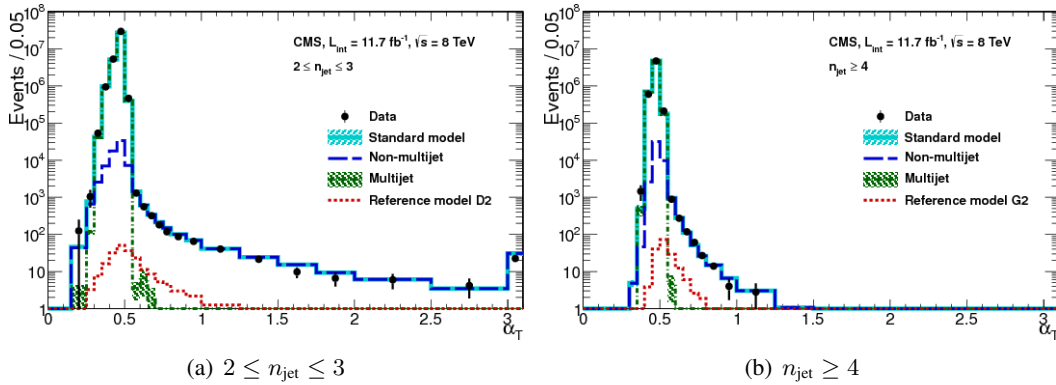


Figure 4: α_T distribution for 11.7 fb^{-1} of data collected at 8 TeV as well as for all standard model backgrounds and one example SUSY signal sample, from [?]. This figure is for illustrative purposes only, as this analysis relies on data control samples to estimate contribution from SM process with genuine E_T .

An extension of α_T can be made for events containing three or more jets by clustering the jets into two pseudo-jets [?]. A pseudo-jet's E_T is calculated as the scalar sum of the contributing jets' transverse energy, while the total transverse energy of the system, H_T , is defined as the scalar sum of the transverse energy of the pseudo-jets: $H_T = E_T^{\text{pj}_1} + E_T^{\text{pj}_2}$. All combinations of the n -jet system are tested, and the configuration which balances the constructed pseudo-jets' E_T is chosen,

ie the combinations which minimizes $\Delta H_T = E_T^{\text{pj}_1} - E_T^{\text{pj}_2}$. As balanced QCD events are expected to have small ΔH_T , this simple clustering criterion provides the best separation between QCD events and events with genuine E_T . Equation (1) can therefore be generalized as:

$$\alpha_T = \frac{1}{2} \times \frac{H_T - \Delta H_T}{\sqrt{H_T^2 - H_T^2}} = \frac{1}{2} \times \frac{1 - (\Delta H_T/H_T)}{\sqrt{1 - (H_T/H_T)^2}}. \quad (4)$$

In the limit that $\Delta H_T \rightarrow 0$, the ratio of missing energy and visible energy can be expressed as a function of α_T :

$$\frac{H_T}{H_T} = \sqrt{1 - \frac{1}{4 \cdot \alpha_T^2}} \quad (5)$$

This analysis uses an α_T threshold of 0.55, which results in accepting events having more than 40% percent as much missing transverse energy as visible transverse energy. For an event with $H_T = 375$ GeV, this amounts to nearly 160 GeV in H_T .

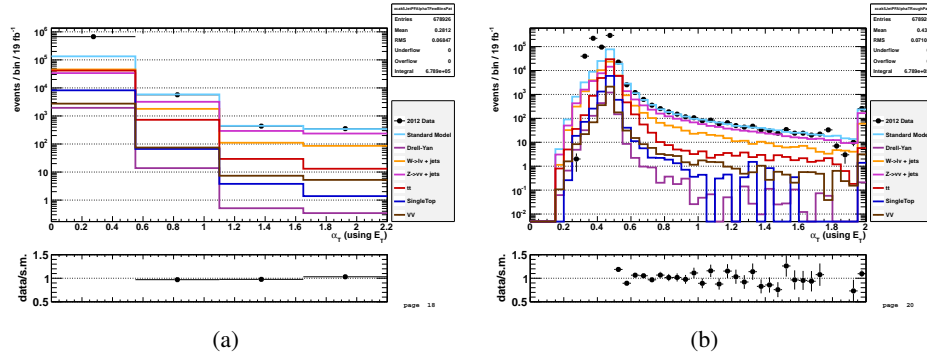


Figure 5: Data–MC comparison of the α_T distribution after following the application of the hadronic pre-selection criteria for events satisfying $n_{\text{jet}} > 2$ and $nb > 0$ in histograms with (a) coarse and (b) fine binning).

4.8 Final selections

After applying the α_T selection described in section 4.7, the remaining events are expected to have little contamination from balanced multi-jet QCD events. Furthermore, QCD events with mismeasured jets are largely rejected since they fall below the α_T threshold. However, two types of rare backgrounds from multi-jet events can lead to values of α_T greater than 0.55. The first is rare circumstance in which several jets with similar values of the azimuthal angle (ϕ) fail to pass the jet p_T threshold. Such jets would not be considered in the calculation of H_T and as a result, they would bias the H_T calculation. The events are rejected by comparing the H_T with the missing transverse energy, E_T^{PF} as defined in 4.3.5, and events with $R_{\text{miss}} = H_T/E_T^{\text{PF}} > 1.25$ are rejected. The second type of rare background is the severe mismeasurement of jets that are absorbed by inefficient crystals in the ECAL. These crystals, which make up 1% of the total crystal count, give only partial record of the energy deposited thereby introducing “fake” H_T in the event. As a filter, the quantity:

$$\Delta\phi^* \equiv \Delta\phi \left(\vec{p}_j, - \sum_{i \neq j} \vec{p}_i \right). \quad (6)$$

ie. the azimuthal distance between a jet and the H_T calculated when not considering the jet, is evaluated for all jets with $p_T > 30$ GeV. Small values of $\Delta\phi^*$ indicate jets that contributed most to the H_T . For each jet with $\Delta\phi^* < 0.5$, the number of dead ECAL cells within $\Delta R(\vec{p}_j, \text{cell}) < 0.3$ is counted. If the number exceeds 9 for any jet, then the event is rejected.

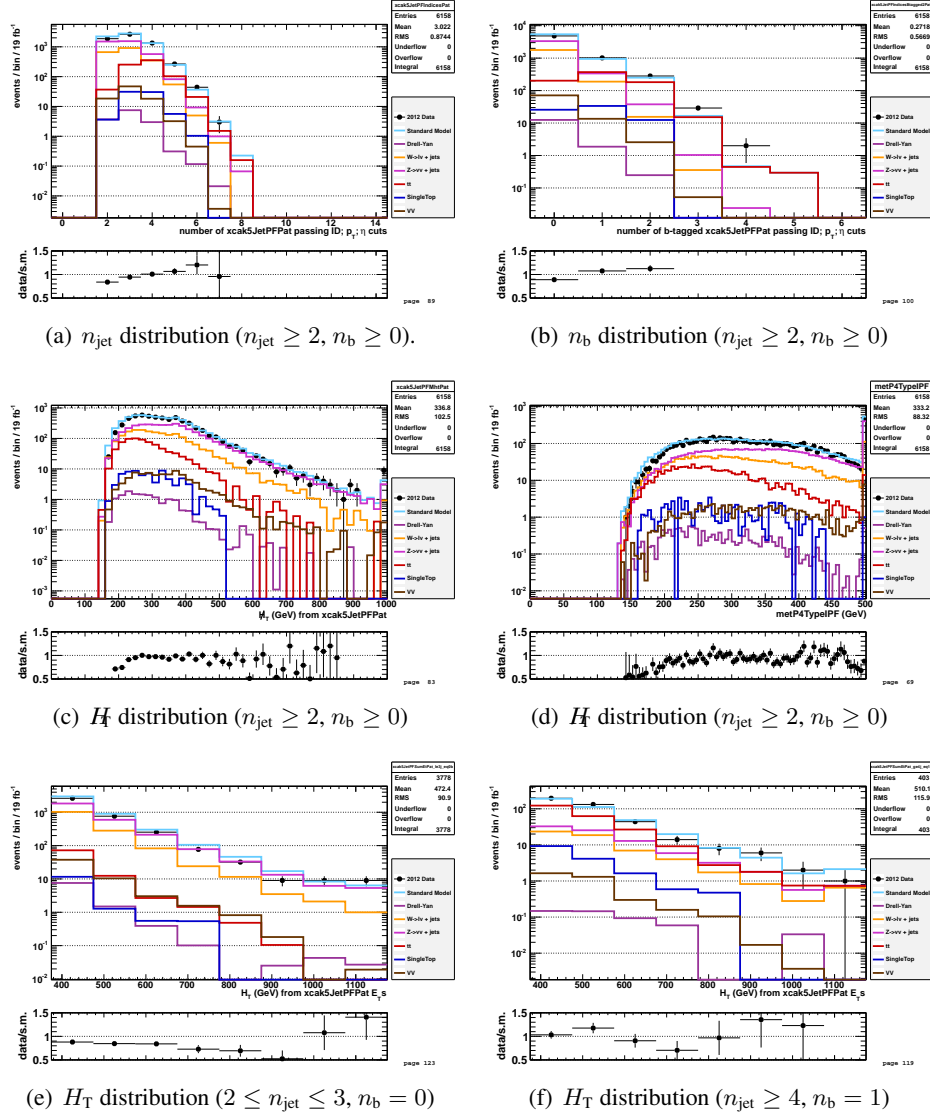


Figure 6: Data–MC comparisons of key variables for the hadronic signal region, following the application of the full signal region selection criteria and the requirements $H_T > 375$ GeV and $\alpha_T > 0.55$: (a) n_{jet} , (b) n_b , (c) H_T , and (d) E_T distributions for an inclusive selection on n_{jet} and n_b , and (e,f) H_T for the two event categories ($2 \leq n_{\text{jet}} \leq 3, n_b = 0$) and ($n_{\text{jet}} \geq 4, n_b = 1$).

5 Background estimation for processes with genuine E_T

After applying the full hadronic selection, the remaining backgrounds are SM processes with genuine E_T in the final state. In the category of zero b-tagged jets, the two primary background are:

- $Z + \text{jets}$; where the Z boson decays into a pair of neutrinos,
- $W + \text{jets}$; where the W boson either undergoes a leptonic decay and the lepton is lost or it undergoes the weak decay $W \rightarrow \tau \nu$ where the τ decays into quarks and

Other SM backgrounds, such as the diboson production, single-top and Drell-Yan are also expected, but at lower yields.

For events with one or more b-tagged jets, the decay of $t\bar{t}$, where each top decays into a b-quark and a W boson which in turn decays into a lost lepton and a neutrino, also becomes a large background source. For events with two reconstructed b-quark jets, $W + \text{jets}$ and $Z + \text{jets}$ are suppressed and $t\bar{t}$ production dominates the background.

This analysis uses a “data-driven” method to estimate backgrounds in the hadronic search region. Data control samples are used to predict background SM yields instead of direct measurement in MC simulations. This approach has two benefits, 1. The beam and detector conditions for the hadronic and control data samples are very similar. 2. The information used from MC simulation is largely in the form of ratios 5.1, which has the benefit of canceling potential systematic effects from simulation.

Two control samples are used to estimate the background. To estimate the $Z \rightarrow \nu\bar{\nu} + \text{jets}$ background, $\gamma + \text{jets}$ events, which have the same kinematic properties as $Z \rightarrow \nu\bar{\nu} + \text{jets}$ when the photon is ignored but different acceptance [? ?], are used. A $\mu + \text{jets}$ control sample is used to estimate all remaining background including the dominant $W + \text{jets}$ and $t\bar{t}$ process.

The final results are obtained through a maximum likelihood fit described in chapter ?? . The following sections describe the estimation method and control selections used in the final fit.

5.1 Overview of the method

For a given bin in H_T , n_{jet} , n_b , the method predicts the number of expected background processes in the hadronic search region ($N_{\text{pred}}^{\text{had}}$) by translating from the observed data yield in a control region ($N_{\text{obs}}^{\text{control}}$) through the use of a *translation factor* (TF) constructed from the ratio of MC hadronic and control yields ie:

$$N_{\text{pred}}^{\text{had}} = \underbrace{\frac{N_{\text{MC}}^{\text{had}}}{N_{\text{MC}}^{\text{control}}}}_{\text{translation factor}} \times N_{\text{obs}}^{\text{control}} \quad (7)$$

In the next step, the expected yield is used rather than the observed yield $N_{\text{obs}}^{\text{control}}$, nonetheless the observed yield is used here for illustration. The sum of expected yields from all MC samples, obtained for the relevant control sample selection, enter the denominator of each transfer factor:

$$N_{\text{MC}}^{\text{control}} = N_W + N_{t\bar{t}} + N_{Z \rightarrow \nu\bar{\nu}} + N_{\text{DY}} + N_{\gamma} + N_{\text{top}} + N_{\text{di-boson}} \quad (8)$$

Depending on the b-tag category, one or both control samples are used to predict the backgrounds in the hadronic search region. For the b-jet multiplicity bins $n_b = 0$ and $n_b = 1$, the $\mu + \text{jets}$ and $\gamma + \text{jets}$ control samples are used to predict the total background. The $\gamma + \text{jets}$ control sample is used to predict the $Z \rightarrow \nu\bar{\nu} + \text{jets}$ background and the expected yield obtained from the $Z \rightarrow \nu\bar{\nu}$ sample enters the numerator of each translation factor:

$$N_{\text{MC}}^{\text{had}}(H_T, n_{\text{jet}}, n_b \leq 1) = N_{Z \rightarrow \nu\bar{\nu}} \quad (9)$$

for the same b-tag categories, The $\mu + \text{jets}$ control sample is used to predict the remaining SM background processes, namely the $W + \text{jets}$, $t\bar{t} + \text{jets}$, Drell-Yan, di-boson and single top backgrounds, and the total expected yield from these processes enter the numerator of each translation factor:

$$N_{\text{MC}}^{\text{had}}(H_{\text{T}}, n_{\text{jet}}, n_{\text{b}} \leq 1) = N_{\text{W}} + N_{t\bar{t}} + N_{\text{DY}} + N_{\text{top}} + N_{\text{di-boson}} \quad (10)$$

Only the μ + jets control sample is used to predict the background. for the b-tag multiplicity bin $n_{\text{b}} = 2$, The γ + jets control sample is not used as the yields in this data control sample is expected to be low due to the requirement of at least two b jets per event. The method of using a W + jets sample to predict the $Z \rightarrow \nu\bar{\nu}$ + jets background has been used previously [? ? ?]. Therefore the total predicted expected yield from all processes are used enter the numerator of each transfer factor:

$$N_{\text{MC}}^{\text{had}}(H_{\text{T}}, n_{\text{jet}}, n_{\text{b}} = 2) = N_{\text{W}} + N_{t\bar{t}} + N_{\text{DY}} + N_{\text{top}} + N_{\text{di-boson}} + N_{Z \rightarrow \nu\bar{\nu}} \quad (11)$$

The control samples used to predict the SM backgrounds for each event category are summarized in Table 9. The control sample selections are described in the subsequent sections.

Table 9: Summary of control samples used to predict the SM background for each event category.

n_{jet}	n_{b}	Control samples
2–3	0	μ + jets, γ + jets
2–3	1	μ + jets, γ + jets
2–3	2	μ + jets
≥ 4	0	μ + jets, γ + jets
≥ 4	1	μ + jets, γ + jets
≥ 4	2	μ + jets

5.2 Definition of the control samples

5.2.1 Muon and photon triggers

Events for the muon control sample are recorded with the HLT_IsoMu24_eta2p1 trigger. Figure 7 (left) shows the HLT_IsoMu24_eta2p1 trigger efficiency as determined in bins of number of primary vertices for muon $p_T > 25$ GeV and $|\eta| < 2.1$ by the muon POG [?]. Figure 7 (right) shows the distribution of the number of vertices in the muon control sample seeded by the HLT_IsoMu24_eta2p1. The efficiency at the mean number of vertices ($n_{Vtx} = 13$) is taken as flat trigger efficiency across n_{jet} , n_b and H_T . This measurement agrees well with direct tag and probe measurements in bins of n_{jet} , n_b , H_T done elsewhere [?].

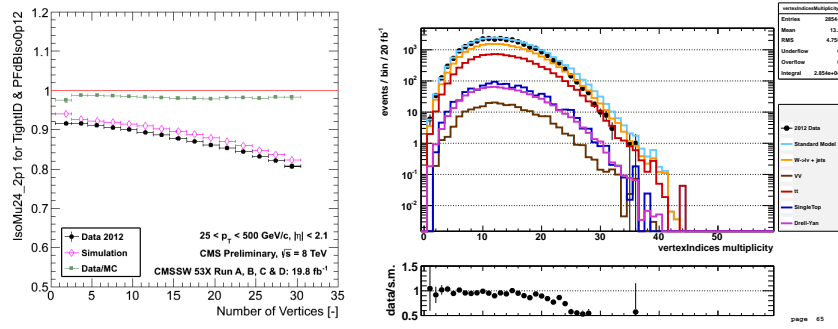


Figure 7: (left) Muon trigger efficiency as a function of number of primary vertices for muon $p_T > 25$ GeV and $|\eta| < 2.1$., (right) number of primary vertices in muon control sample.

Events for the photon control sample are recorded with the HLT_Photon150 trigger, which is $\sim 100\%$ efficient for $E_T^{\text{photon}} > 165$ GeV and $H_T > 375$ GeV, as shown in Figure 8. The efficiency measurement is made using the HLT_Photon90 trigger as a reference.

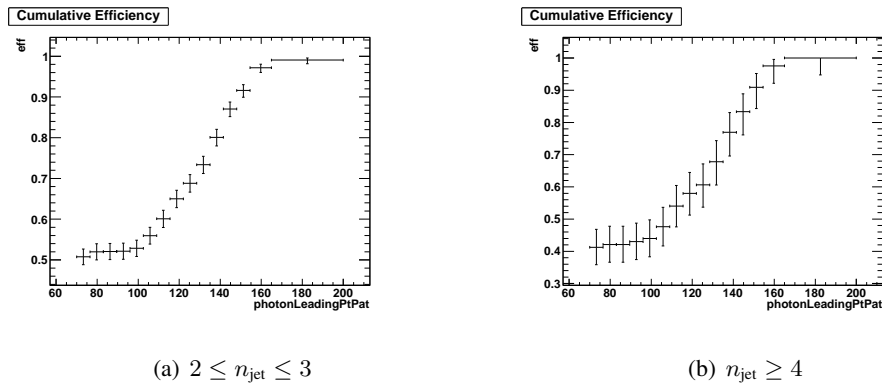


Figure 8: Cumulative efficiency turn-on curves for the HLT_Photon150 trigger as a function of photon p_T for events satisfying $2 \leq n_{\text{jet}} \leq 3$ (left) and $n_{\text{jet}} \geq 4$ (right).

5.2.2 The μ + jets control sample

W + jets and $t\bar{t}$ processes are found in the hadronic search region when the decay lepton is missed by the lepton veto, either because it was not reconstructed properly, fell out of acceptance or alternatively, decayed hadronically in the case of a tau lepton from a high- p_T W boson. Instead of directly relying on MC simulation to estimate these background, a μ + jets control sample is used where the selection criteria is chosen to identify W bosons decaying to a muon and a neutrino. Then by removing the muon from the event, one effectively selects a sample of W boson decaying to a neutrino and a lost lepton. In order to select events containing W bosons, exactly one tight isolated muon 4.3 within an acceptance of $p_T > 30$ GeV and $|\eta| < 2.1$ is required, and the transverse mass of the W candidate, $M_T = \sqrt{2p_T^\mu E_T(1 - \cos(\Delta\phi(\vec{p}^\mu, \vec{E}_T)))}$ must be between 30 and 125 GeV. Events are vetoed if a muon is found inside a jet, i.e. $\Delta R(\mu, \text{jet}) < 0.5$. The single isolated track veto, described in sections 4.3.6 and 4.5, is applied. The veto considers all single isolated tracks in the event except that associated with the identified, isolated muon. The cleaning cut H_T/E_T^{PF} described in ?? is also applied, where the E_T^{PF} is adjusted to exclude the muon's transverse momentum. This modification ensures that the quantities H_T and E_T^{PF} can be compared. Lastly, while all other jet-based quantities, like H_T and H_T , are kept consistent with those applied in the hadronic search region, the α_T requirement is removed. This modification increases the statistical power of the sample. Removing the α_T requirement is only made possible by the control sample's kinematic cuts which ensure the selection of electroweak processes while keeping contamination from multi-jet QCD events negligible. Because the control sample is used to extrapolate yields in a hadronic search region, which includes the α_T requirement, a closure test as been devised and explained in ?? to demonstrate that no significant biases is seen from the exclusion of the α_T cut.

5.2.3 The γ + jets control sample

The $Z \rightarrow \nu\bar{\nu}$ + jets background is estimated using γ + jets events which have a higher cross-section but similar kinematic properties as $Z \rightarrow \nu\bar{\nu}$ + jets when the photon is ignored [? ?]. The γ + jets sample is obtained by requiring exactly one tightly identified and isolated photon (as defined in section 4.3) with a transverse momentum of at least 165 GeV. The photon is required to be contained within the barrel of the detector, ie $|\eta_\gamma| < 1.44$, and to not overlap with any reconstructed jets ($\Delta R(\gamma, \text{jet}) < 1.0$.) As in the muon control sample, the \vec{E}_T is modified to exclude the photon when imposing the $H_T/E_T^{\text{PF}} < 1.25$ selection cut. All other selections are consistent with the hadronic search region including the $\alpha_T > 0.55$ cut.

6 Closure tests and systematic uncertainties on transfer factors

Limitations in simulating detector effects and event kinematics requires us to apply appropriate systematic uncertainties on the simulation-based translation factors. The following section describes how we obtain these uncertainties through the method of closure tests.

6.1 Closure tests

At its core, the method compares an observed yield (N_{obs}) and a predicted yield (N_{pred}) in a sub-sample of a control region. The predicted yield is constructed by translating from a statistically independent data sample to the data sample of interest by the use of the proper translation factor. For example, in a given H_T bin, a prediction for the $n_{\text{jet}} \geq 4$, $n_b = 1$, $\mu + \text{jets}$ sample can be made by translating from the $2 \leq n_{\text{jet}} \leq 3$, $n_b = 1$, $\mu + \text{jets}$ in data via the translation factor:

$$\frac{N_{\text{MC}}^{\mu+\text{jets}}(H_T, n_{\text{jet}} \geq 4, n_b = 1)}{N_{\text{MC}}^{\mu+\text{jets}}(H_T, 2 \leq n_{\text{jet}} \leq 3, n_b = 1)} \quad (12)$$

The agreement between N_{obs} and N_{pred} is expressed as $(N_{\text{obs}} - N_{\text{pred}})/N_{\text{pred}}$. Assuming only statistical uncertainties on N_{obs} and N_{pred} , deviation of the ratio from zero defines our level of closure. A closure test set is defined as ratios for each H_T bin. Looking at the ratio as a function of H_T allows the measurement of statistical significant biases from zero and/or any dependence on H_T . If statistically significant biases are observed, further studies are required to understand and correct for these biases.

Eight sets of closure tests probe key ingredients of the simulation modeling of the SM backgrounds with genuine E_T as a function of H_T , as shown in Fig. 9. This is done for the two jet multiplicity bins separately: (a) $2 \leq n_{\text{jet}} \leq 3$ and (b) $n_{\text{jet}} \geq 4$.

Under the assumption of closure for the full ensemble of tests, systematic uncertainties on the transfer factors are derived for each n_{jet} category and H_T regions. The treatment for estimating the

systematic uncertainties on the transfer factors is described in Section 6.2.

As described in section ?? The α_T requirement is not imposed in the μ + jets control sample. Therefore it is important to verify the approach of using μ + jets samples without an α_T requirement to make background predictions in the signal region. The first set of closure tests (denoted by circles) attempts to do this by probing the modeling of the α_T distribution in genuine E_T events as a function of H_T . The tests compares data yields in the μ + jets sample with an α_T requirement against predictions determined in a μ + jets sample with the α_T requirement inverted.

The next three sets (triangles, crosses, squares) probe the sensitivity of the transfer factors to the relative admixture of events from the W + jets and $t\bar{t}$ processes. These tests are conservative, since by construction, the admixture changes little when translating from the μ + jets control region to the signal region, whereas the closure tests use sub-samples with different b-tag requirements and therefore have very different admixtures of W + jets and $t\bar{t}$ events. In the $2 \leq n_{\text{jet}} \leq 3$ bin, the test is sub-divided into separate jet categories. These tests also probe the modeling of the reconstruction of b-quark jets, although this also addressed more fully by dedicated studies that determine systematic uncertainties via the method described in Sec. ??.

The remaining tests probe the simulation modeling of the jet multiplicity in the μ + jets and γ + jets samples, which is checked due to the exclusive binning in jet multiplicity. As in the case of the W + jets / $t\bar{t}$ admixture, this set of tests is a very conservative check, as predictions are always made from the same jet multiplicity bin, whereas the closure tests translate between the two bins.

Tables 10 and 11, which summarize the results obtained from fits of zeroth order polynomials (i.e. a constant) to the sets of closure tests performed in the $2 \leq n_{\text{jet}} \leq 3$ and $n_{\text{jet}} \geq 4$ bins. Table 12 lists the fits result common to both jet multiplicities. The best fit value and its uncertainty is listed for each set of closure tests, along with the χ^2 , the number of degrees of freedom, and the p-value of the fit. The best fit value for the constant parameter is indicative of the level of closure, as averaged across the full H_T range considered in the analysis, and the p-value is indicative of

whether there is any significant dependence on H_T .

The closure tests demonstrate, within the statistical precision of each test, that there are no significant biases or dependencies on H_T inherent in the transfer factors obtained from simulation.

One set of tests does indicate a poor goodness of fit (indicated by a low p-value), which is the $n_b = 0 \rightarrow n_b = 1$ test in the $\mu + \text{jets}$ sample for the $n_{\text{jet}} \geq 4$ category, which has been identified as a upward (downward) fluctuation of event counts in the H_T bin 475–575 GeV (575–675 GeV) when $n_b = 1$. Combining these two bins yields an acceptable fit result, as indicated in Table 11, which points to a simple fluctuation rather than any systematic bias.

Table 10: A summary of the results obtained from fits of zeroth order polynomials (i.e. a constant) to four sets of closure tests performed in the $2 \leq n_{\text{jet}} \leq 3$ bin.

Closure test	Symbol	Constant fit			
		Best fit value	χ^2	d.o.f.	p-value
$\alpha_T < 0.55 \rightarrow \alpha_T > 0.55$ ($\mu + \text{jets}$)	Circle	0.007 ± 0.02	3.91	7	0.79
1 b-tags \rightarrow 2 b-tags ($\mu + \text{jets}$, nJet=3)	Triangle	-0.008 ± 0.04	3.20	7	0.87
0 b-tags \rightarrow 1 b-tags ($\mu + \text{jets}$, nJet=2)	Cross	0.111 ± 0.03	5.87	7	0.55
0 b-tags \rightarrow 1 b-tags ($\mu + \text{jets}$, nJet=3)	Square	0.040 ± 0.02	1.12	7	0.99

Table 11: A summary of the results obtained from fits of zeroth order polynomials (i.e. a constant) to three sets of closure tests performed in the $n_{\text{jet}} \geq 4$ bin. [†]Further explanation of this fit can be found in the text.

Closure test	Symbol	Constant fit			
		Best fit value	χ^2	d.o.f.	p-value
$\alpha_T < 0.55 \rightarrow \alpha_T > 0.55$ ($\mu + \text{jets}$)	Circle	0.011 ± 0.04	5.81	7	0.56
1 b-tags \rightarrow 2 b-tags ($\mu + \text{jets}$)	Triangle	0.045 ± 0.03	9.36	7	0.23
0 b-tags \rightarrow 1 b-tags ($\mu + \text{jets}$)	Square	0.007 ± 0.03	25.30	7	0.00
0 b-tags \rightarrow 1 b-tags ($\mu + \text{jets}$) [†]	Square	0.009 ± 0.03	10.12	6	0.12

Table 12: A summary of the results obtained from fits of zeroth order polynomials (i.e. a constant) to four sets of closure tests ($2 \leq n_{\text{jet}} \leq 3 \rightarrow n_{\text{jet}} \geq 4$) that probe the accuracy of the MC modeling of the n_{jet} distribution observed in data, using the three data control samples.

Closure test	Symbol	Constant fit			
		Best fit value	χ^2	d.o.f.	p -value
$2 \leq n_{\text{jet}} \leq 3 \rightarrow n_{\text{jet}} \geq 4$ (μ + jets, 1 b-tags)	Times	-0.053 ± 0.03	8.02	7	0.33
$2 \leq n_{\text{jet}} \leq 3 \rightarrow n_{\text{jet}} \geq 4$ (μ + jets, 1 b-tags)	Invert. Triangle	0.018 ± 0.04	6.23	7	0.51
$2 \leq n_{\text{jet}} \leq 3 \rightarrow n_{\text{jet}} \geq 4$ (μ + jets, 0 b-tags)	Star	0.034 ± 0.02	9.24	7	0.24
$2 \leq n_{\text{jet}} \leq 3 \rightarrow n_{\text{jet}} \geq 4$ (γ + jets, 0 b-tags)	Diamond	0.100 ± 0.04	12.20	7	0.09

6.2 Systematic uncertainties from closure tests

Once it is established that no significantly large bias or trend is observed for any set of closure tests, then systematic uncertainties are determined.

Systematics uncertainties are determined for each H_T bin, as indicated in Table 13. For each H_T region, the systematic uncertainty is estimated by taking the quadrature sum of the weighted mean and sample variance for the closure tests within the given H_T region. This procedure yields the values quoted in Table 13.

As the closure tests do not translate from control region to signal region, they do not probe the uncertainty in the signal trigger efficiencies. To account for this, a trigger uncertainty of 5% is added in quadrature to the uncertainty values obtained via the closure tests and the total is summarized in Table 14.

Table 13: A summary of the magnitude of the systematic uncertainties (%) obtain from closure tests, according to n_{jet} and H_T region.

n_{jet}	H_T region (GeV)							
	375–475	475–525	525–675	675–775	775–875	875–975	1075–1075	> 1175
2–3	3	4	5	11	11	16	16	16
≥ 4	3	4	6	13	13	13	13	20

Figure 9 shows the sets of closure tests overlaid on top of gray bands that represent the H_T -

Table 14: A summary of the magnitude of the total systematic uncertainties (%) assigned to the transfer factors, according to n_{jet} and H_T region.

n_{jet}	H_T region (GeV)							
	375–475	475–525	525–675	675–775	775–875	875–975	1075–1075	> 1175
2–3	6	6	7	12	12	17	17	17
≥ 4	6	6	8	14	14	14	14	21

dependent systematic uncertainties in Table 13. These systematic uncertainties are assumed to fully uncorrelated between the different b jet multiplicity categories and also the eight H_T regions, which is a conservative approach given that one can expect some correlation between adjacent H_T bins (due to comparable kinematics).

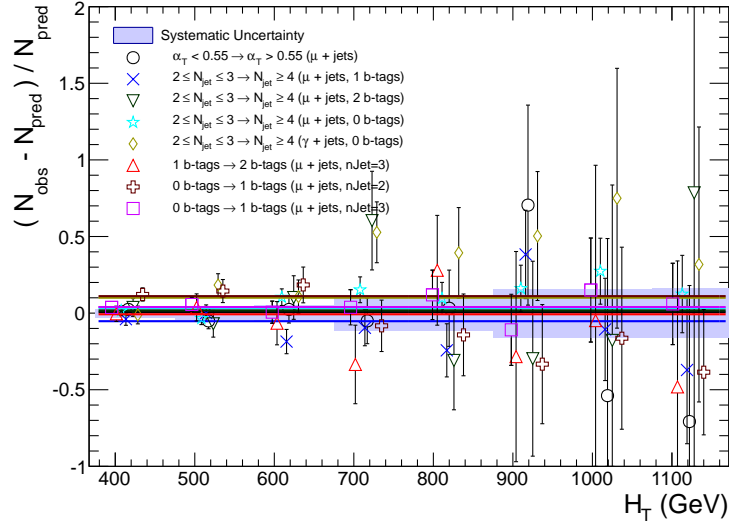
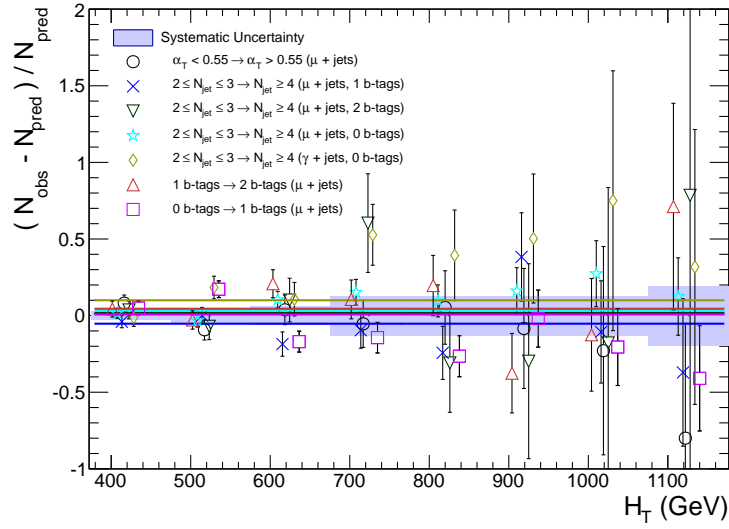
(a) $2 \leq n_{\text{jet}} \leq 3$ (b) $n_{\text{jet}} \geq 4$

Figure 9: Sets of closure tests (open symbols) overlaid on top of the systematic uncertainty used for each of the H_T region (shaded bands) and for the two different jet multiplicity bins: (a) $2 \leq n_{\text{jet}} \leq 3$ and (b) $n_{\text{jet}} \geq 4$.

7 Signal models and efficiencies

7.1 Introduction

As described in section 1.2, SUSY is a theory of many particles and parameters. In order to provide experiments with clear detectable signatures to search for, simplified models (SMS) have been derived [?] which reduce both particles and parameters. In this work, the results are interpreted in two SMS models:

- T2cc: pair produced stop sparticles each decaying into a charm quark and a neutralino
- T2tt: pair produced stop sparticles each decaying into a top quark and a neutralino.

SMS MC samples are generated at leading order with MADGRAPH [?] by the CMS SUSY MC group and binned in stop mass (m_{Stop}) and neutralino mass (m_{LSP}). The analysis efficiency is studied in the usual n_{jet} , n_b , H_T , binning but due to computational limitations not all categories are used to set a limit on a given model. The choice of categories for a model is made by computing the expected upper limit on the signal cross-section for each category separately using the much quicker asymptotic method [1]. The categories are ranked by their expected upper limit. Depending on the number of mass bins and number of events per bin, two or more categories with the highest rank are chosen. The simplified models, along with the event categories considered for each, is summarised in Table 15.

Table 15: A summary of the simplified models considered for interpretation. The event categories considered for each model are listed.

Model	Production/decay mode	(n_{jet}, n_b) event categories considered
T2cc	$pp \rightarrow \tilde{t}\tilde{t}^* \rightarrow c\tilde{\chi}^0 \bar{c}\tilde{\chi}^0$	$(2-3,0), (\geq 4,0), (\geq 4,1)$
T2tt	$pp \rightarrow \tilde{t}\tilde{t}^* \rightarrow t\tilde{\chi}^0 \bar{t}\tilde{\chi}^0$	$(\leq 3,1), (\leq 3,2)$

7.2 Efficiency times acceptance

The signal efficiency times acceptance is measured in the same binning as the analysis binning (n_{jet}, n_b, H_T). To reduce the number of figures in this section to a manageable level, only the total efficiency for the relevant event categories and inclusive selection on H_T (> 375 GeV) is shown. Figures 10 and 11 show the expected signal efficiency times acceptance for the hadronic selection the T2cc and T2tt interpretations for categories of interest.

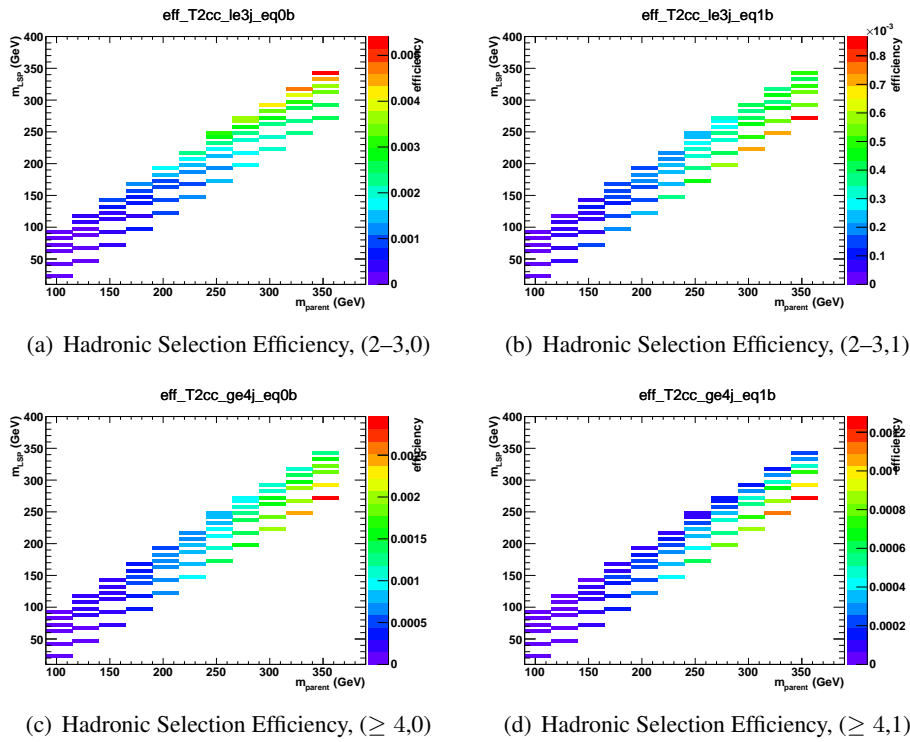


Figure 10: Hadronic selection efficiency times acceptance for T2cc for the relevant event categories defined by n_{jet} and n_b . Note the different z-axis scales.

In T2cc, the decay quarks become virtually undetectable as the nearly degenerate parent and daughter masses leave little energy for the decay products. Therefore any analysis interpreting in the T2cc model relies on hard- p_T jets from initial state radiation for acceptance. The efficiency times

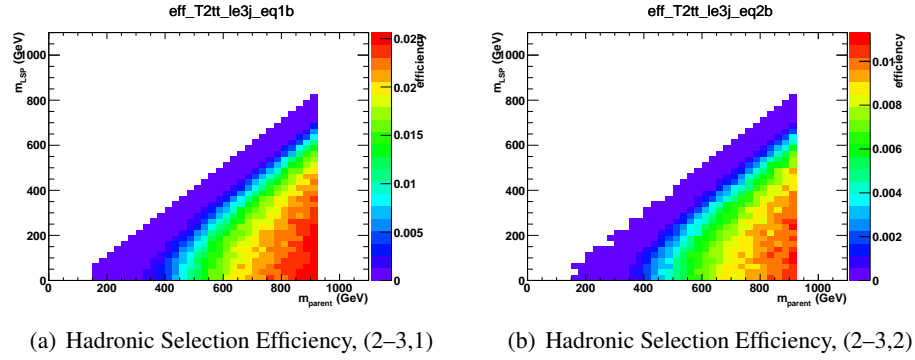


Figure 11: Hadronic selection efficiency times acceptance for the T2tt for the relevant event categories defined by n_{jet} and n_b . Note the different z-axis scales.

acceptance is below the percent level where The largest efficiencies for the smallest mass splittings, $\Delta M = \sim 10$ GeV, are obtained with the (2–3,0) category, while for larger mass splittings the (2–3,1), ($\geq 4,0$), and ($\geq 4,1$) categories contribute due to the reduced backgrounds in these categories. In T2tt the largest efficiencies are obtained in largest mass splittings in both categories of interest. In both models, the signal efficiency in the $\mu + \text{jets}$ control sample is negligible with respect to the signal region.

8 Systematic uncertainties on signal efficiency times acceptance

8.1 Introduction

To gain statistical power, The systematic uncertainty in the signal acceptance times efficiency is determined per mass point per event category ($n_{\text{jet}}, n_{\text{b}}$), but inclusively in H_T . This section details the methods used to determine the magnitude of the systematic uncertainties to be applied. Four sources of uncertainty are measured: the jet energy scale, the parton distribution functions, initial state radiation and b-tag scale factors. Three other uncertainties are quoted: the uncertainty in the luminosity (2.6%) and trigger (5%) measurements and the “dead ECAL” filter (3 %) used in the candidate signal event selection. Each contribution is considered to be independent and all contributions are summed in quadrature to obtain a total systematic uncertainty per mass point per category.

The following sub-sections provide an overview of the various sources of uncertainty, before details on specific models are provided.

8.2 PDF uncertainties

The simulated signal events were produced with the CTEQ6L1 PDF set by default. As recommended by PDF4LHC [?], the uncertainty in signal efficiency due to knowledge of the PDFs is obtained by comparing the signal efficiency with that obtained with three newer alternative PDF sets: CT10, NNPDF2.1, and MSTW2008. Using the envelope formula in the reference, a single efficiency is calculated from the three alternate PDF sets.

Figures 21 and 26 (Appendix C) show the relative difference of the signal efficiency times acceptance for the central value of the envelope calculation and the nominal PDF (CTEQ6L1) set used to produce the signal samples. The relative difference is taken as a symmetric systematic uncertainty, which varies in absolute terms within the range 0–10% in both models depending

on the category of interest.

8.3 Jet energy scale

Figures 22 and 27 (Appendix C) show the relative change in the signal efficiency times acceptance for the relevant categories for the T2cc and T2tt interpretations when varying the energy of all jets in an event up or down according to a p_T - and η -dependent jet energy scale uncertainty, as recommended by the JetMET POG. In T2cc, larger variations are observed for the higher jet multiplicity category, as the jets are softer for the same requirement on H_T . Also, the variations may increase with increasing mass splitting as additional (soft) jets from the decay become hard enough to move within acceptance. The variations in both signal models range between $\sim 5\%$ and $\sim 15\%$ for the low and high jet multiplicity, and are largely independent of parent and daughter sparticle mass.

8.4 Initial state radiation

Signal samples produced with MADGRAPH exhibit discrepancies that have been attributed to the mismodelling of initial state radiation. These discrepancies are corrected as recommended by the SUSY PAG [?]. As per prescription, events are reweighted according to the vectorial sum of the momenta of the pair-produced sparticles. The sparticle-system p_T dependent weights are summarized in Table 16. In addition to the central weight, further variations about the central weight according to the uncertainty in the weight is applied in order to determine the systematic uncertainty associated with the correction. The resulting systematic uncertainties are largest near the diagonal where selected events contain significant amounts of boost due to the presence of initial state radiation.

Figure 23 and 28 (Appendix C) shows the relative change in the signal efficiency times acceptance for the relevant categories for the T2cc and T2tt interpretation when varying up and down

the sparticle system p_T -dependent corrections by their uncertainties. The largest variations, up to $\sim 25\%$ are observed for the smallest mass splittings, when the reliance on ISR jets for acceptance is largest.

Table 16: Sparticle system p_T dependent corrections and systematic weight variations.

Sparticle system p_T (GeV)	Central Weight	Systematic Variation
$0 < p_T < 120$	1.00	± 0.0
$120 < p_T < 150$	0.95	± 0.05
$150 < p_T < 250$	0.90	± 0.10
$p_T > 250$	0.80	± 0.20

8.5 b-tag scale factor corrections

The uncertainty on the btag scale factors described in section [REF] is calculated by varying the scale factors up and down by their uncertainty as described in Ref. [?].

Figure 24 and 29 (Appendix C) show the relative change in the signal efficiency times acceptance for the relevant categories for the T2cc and T2tt interpretations when varying up and down the scale-factor corrections by their uncertainties. The variations are anti-correlated for the two n_b categories used by this interpretation and are generally small, at the level of 1–5%, with respect to other contributions.

8.6 Total systematic uncertainties

A few mass bins exhibit large uncertainties compared to neighboring mass bins. This effect attributed to low statistics when calculating the signal efficiency times acceptance in that bin. In order to decouple systematic and statistical uncertainties, these values have been replaced with appropriate values (determined by neighboring bins) in the calculation of the total uncertainty. Hence, figures 25 and 25, representing the total systematic uncertainty in the T2cc and T2tt interpretations for relevant categories are devoid of such fluctuations.

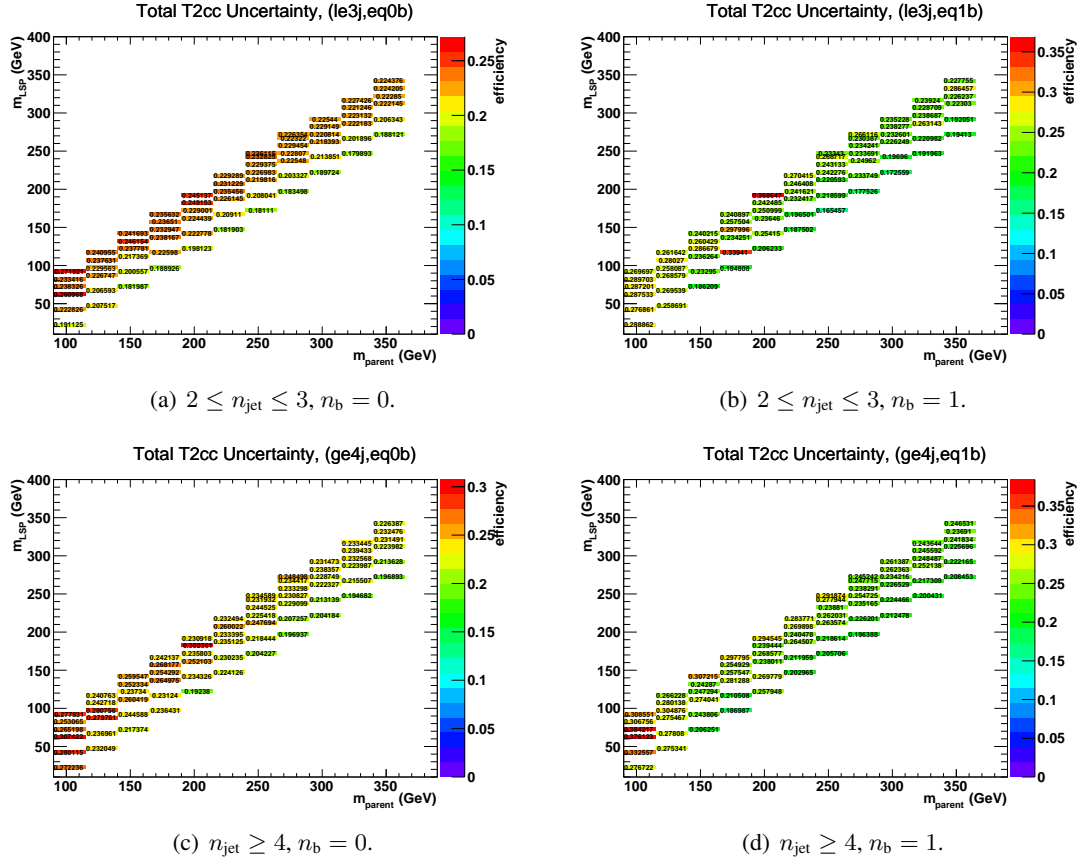


Figure 12: The total systematic uncertainty in the signal efficiency times acceptance for all relevant event categories for the T2cc interpretation.

Table 18 presents a *representative* range of values for the contribution to the total systematic uncertainty in the signal efficiency times acceptance for each relevant event category. An uncertainty of 2.6% in the integrated luminosity is also considered. An uncertainty of 5% from the trigger uncertainty measurement Figure 25 shows the total systematic uncertainty in the T2cc mass plane for the relevant categories.

input statistics

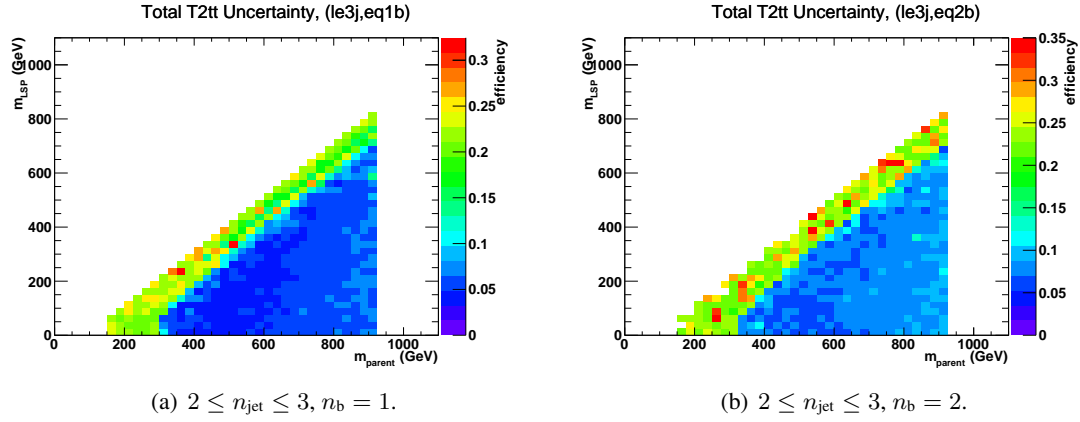


Figure 13: The total systematic uncertainty in the signal efficiency times acceptance for all relevant event categories for the T2tt interpretation.

Table 17: Representative ranges for each contribution to the total systematic uncertainty in the signal efficiency times acceptance for each relevant event category for the T2cc interpretation.

Category	(2–3,0)		(≥ 4,0)		(≥ 4,1)		(≥ 2, ≥ 0)	
Range	Min.	Max.	Min.	Max.	Min.	Max.	Min.	Max.
PDF	0.00	0.05	0.00	0.05	0.00	0.10		
JES	0.00	0.10	0.00	0.10	0.00	0.15		
ISR	0.15	0.25	0.10	0.15	0.15	0.30		
b-tag SF	0.00	0.08	0.00	0.10	0.00	0.15		
Luminosity							0.026	0.026
Trigger							0.05	0.05
Dead Ecal							0.03	0.03
Total syst	0.18	0.25	0.19	0.30	0.20	0.38		

Table 18: Representative ranges for each contribution to the total systematic uncertainty in the signal efficiency times acceptance for each relevant event category for the T2tt interpretation.

Category	(2–3,1)		(2–3,2)		$(\geq 2, \geq 0)$	
Range	Min.	Max.	Min.	Max.	Min.	Max.
PDF	0.00	0.10	0.00	0.10		
JES	0.00	0.10	0.00	0.05		
ISR	0.00	0.20	0.00	0.22		
b-tag SF	0.00	0.05	0.00	0.10		
Luminosity					0.026	0.026
Trigger					0.05	0.05
Dead Ecal					0.03	0.03
Total syst	0.05	0.25	0.05	0.30		

9 Results

The likelihood described in ref:likelihood is used to relate yields, uncertainties. It is constructed using ROOTFIT [?] and maximized using MINUIT [?].

9.1 Standard Model

To test compatibility with a Standard Model only hypothesis, the signal term is removed from the likelihood model. The parameter values maximizing the likelihood function are listed in Tables 20–25 found in Appendix A. The resulting SM yields along with the observed data yields are summarized in Tables B. The uncertainty on the yields are obtained by constructing a probability density function (p.d.f) from the maximized likelihood, then generating an ensemble of pseudo-experiments from this p.d.f. and maximizing the same likelihood form for each pseudo-experiment, resulting in an ensemble of yields. The 68% quantile of each ensemble defines the quoted uncertainty on the corresponding yield.

Figures 15–20 show the H_T -binned observed data yields (black filled circles) and the SM expectations and uncertainties (dark blue solid line with light blue bands) as determined by the fit for the hadronic signal region and the $\mu + \text{jets}$ or both ($\mu + \text{jets}, \gamma + \text{jets}$) control samples, depending on the event category. The uncertainties in the SM expectations obtained from the ensemble of pseudo-experiments reflect the statistical uncertainties in the considered data samples and the systematic uncertainties in the transfer factors as discussed in section 6. Figures 15–20 are summarized in tabular format in Tables 26–31 in appendix B along with observed data yields and the fit result for all event categories and both signal region and control sample bins.

For each n_b, n_{jet} category, the goodness-of-fit of the SM-only hypothesis is determined by considering simultaneously all H_T bins entering the likelihood. The goodness-of-fit described in [?] is obtained by comparing the nominal maximized likelihood value $L_{\text{max}}^{\text{data}}$ to the corresponding ensemble of values, L_{max} . The quantile which $L_{\text{max}}^{\text{data}}$ falls in the distributions is interpreted as a

p-value. A p-value derived from a chi-square is also plotted for comparison.

The p-values obtained, shown in Figure 14 (Left), are found to be uniformly distributed in the range 0.0–1.0, with the lowest p-value determined to be 0.17.

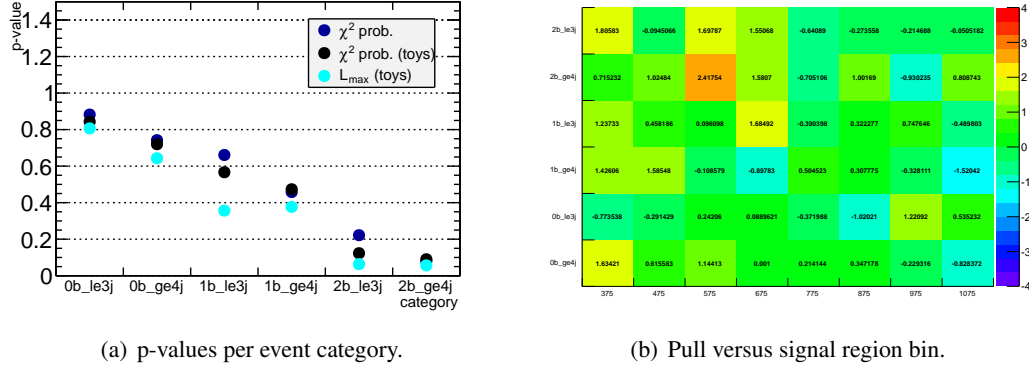


Figure 14: Pulls and p-values. See text for details

Table 19: Summary of hadronic yields from fit.

	375–475	475–575	575–675	675–775	775–875	875–975	975–1075	1075– ∞
0b le3j SM	2744^{+48}_{-43}	771^{+21}_{-23}	254^{+13}_{-13}	$76.5^{+6.1}_{-4.8}$	$33.7^{+3.7}_{-3.8}$	$11.8^{+1.9}_{-2.1}$	$6.3^{+1.4}_{-1.3}$	$3.2^{+1.0}_{-0.9}$
0b le3j Data	2728	766	257	77	32	9	9	4
1b le3j SM	426^{+15}_{-17}	114^{+6}_{-6}	$35.5^{+3.3}_{-2.8}$	$10.1^{+1.4}_{-1.5}$	$3.7^{+0.9}_{-0.8}$	$1.6^{+0.7}_{-0.6}$	$0.5^{+0.3}_{-0.4}$	$0.1^{+0.1}_{-0.0}$
1b le3j Data	444	118	36	15	3	2	1	0
2b le3j SM	$65.0^{+4.3}_{-4.3}$	$18.4^{+1.7}_{-1.6}$	$4.2^{+0.6}_{-0.5}$	$1.1^{+0.3}_{-0.2}$	$0.2^{+0.1}_{-0.1}$	$0.0^{+0.0}_{-0.0}$	$0.0^{+0.0}_{-0.0}$	$0.0^{+0.0}_{-0.0}$
2b le3j Data	78	18	8	3	0	0	0	0
0b ge4j SM	456^{+15}_{-14}	291^{+12}_{-12}	148^{+8}_{-7}	$66.0^{+5.6}_{-5.2}$	$27.1^{+2.9}_{-3.4}$	$14.0^{+1.9}_{-2.1}$	$6.5^{+1.5}_{-1.2}$	$3.2^{+1.0}_{-0.9}$
0b ge4j Data	480	299	158	66	28	15	6	2
1b ge4j SM	190^{+10}_{-8}	120^{+6}_{-5}	$45.6^{+3.1}_{-3.8}$	$17.1^{+2.6}_{-1.9}$	$6.8^{+1.5}_{-1.3}$	$5.4^{+1.3}_{-1.6}$	$2.4^{+0.9}_{-0.9}$	$1.2^{+0.7}_{-0.8}$
1b ge4j Data	206	135	45	14	8	6	2	0
2b ge4j SM	$73.6^{+4.2}_{-4.2}$	$45.7^{+2.8}_{-2.9}$	$20.4^{+1.8}_{-1.8}$	$7.7^{+1.2}_{-1.0}$	$1.9^{+0.3}_{-0.3}$	$0.9^{+0.2}_{-0.2}$	$0.4^{+0.1}_{-0.1}$	$0.4^{+0.1}_{-0.2}$
2b ge4j Data	79	52	31	12	1	2	0	1

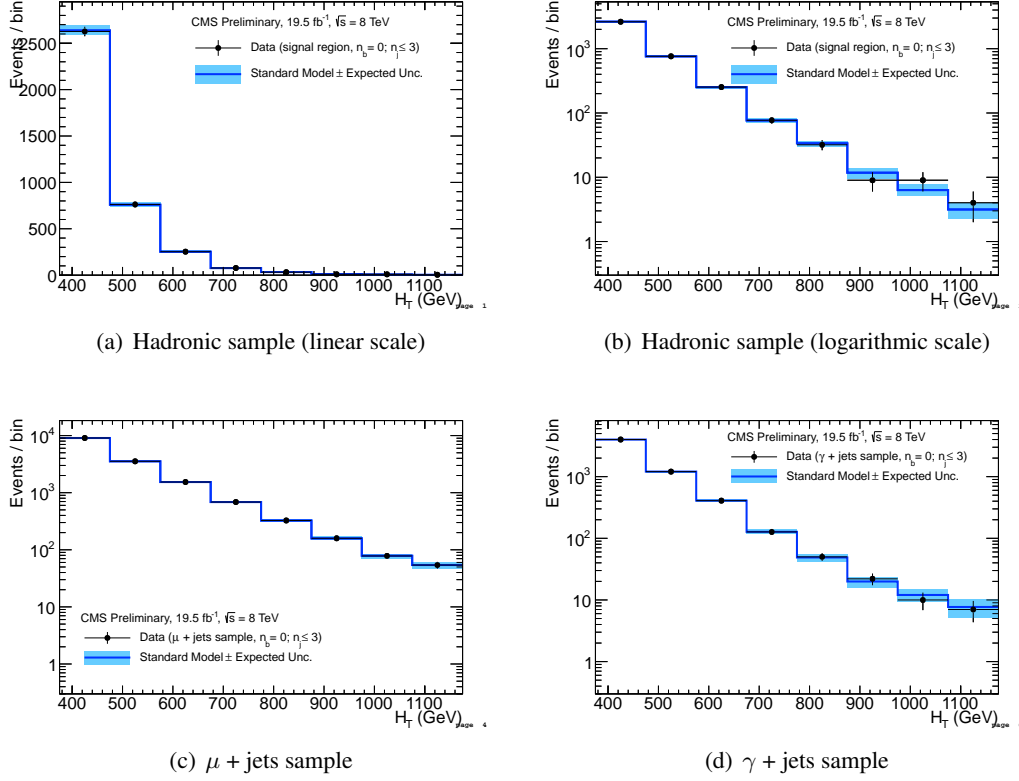


Figure 15: Comparison of the H_T -binned observed data yields and SM expectations when requiring $2 \leq n_{\text{jet}} \leq 3$ and $n_b = 0$ for the (a-b) hadronic, (c) μ + jets, (d) $\mu\mu$ + jets and (e) γ + jets samples, as determined by a simultaneous fit to all data samples under the SM-only hypothesis. The observed event yields in data (black dots) and the expectations and their uncertainties (dark blue solid line with light blue bands), as determined by the simultaneous fit, are shown. For illustrative purposes only, the signal expectations (pink dashed line) for the model T2cc with $m_{\tilde{q}} = 250$ GeV and $m_{\text{LSP}} = 240$ GeV are stacked on top of the SM expectations.

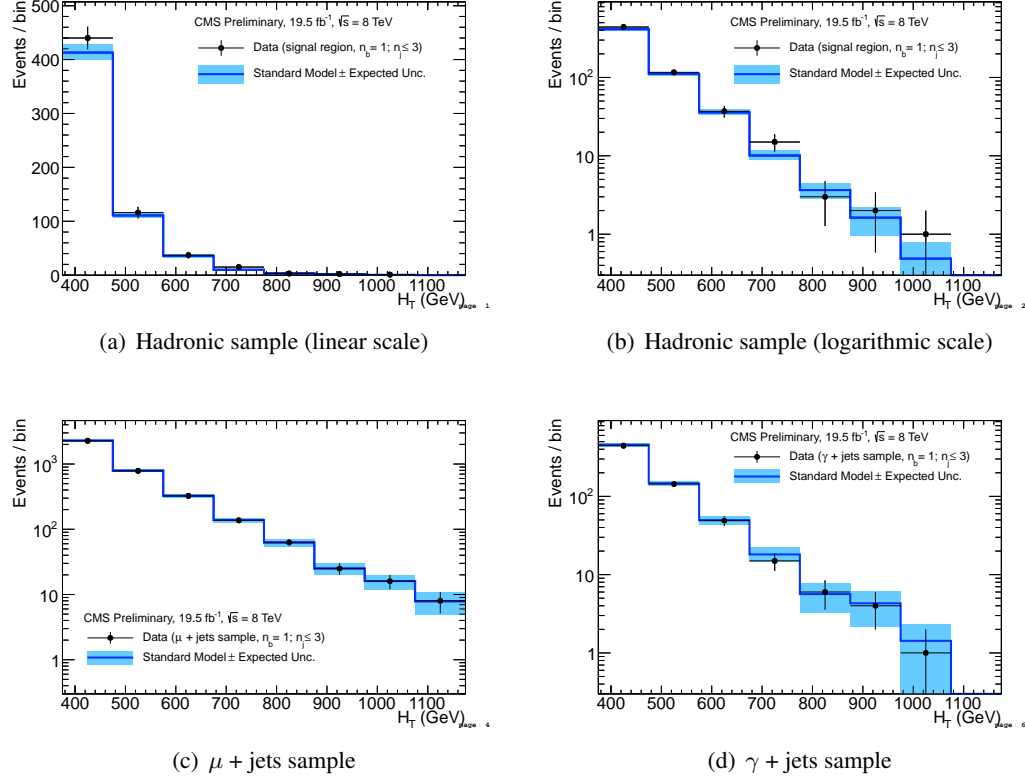


Figure 16: Comparison of the H_T -binned observed data yields and SM expectations when requiring $2 \leq n_{\text{jet}} \leq 3$ and $n_b = 1$ for the (a-b) hadronic, (c) μ + jets, (d) $\mu\mu$ + jets and (e) γ + jets samples, as determined by a simultaneous fit to all data samples under the SM-only hypothesis. The observed event yields in data (black dots) and the expectations and their uncertainties (dark blue solid line with light blue bands), as determined by the simultaneous fit, are shown. For illustrative purposes only, the signal expectations (pink dashed line) for the model T2cc with $m_{\tilde{q}} = 250$ GeV and $m_{\text{LSP}} = 170$ GeV are stacked on top of the SM expectations.

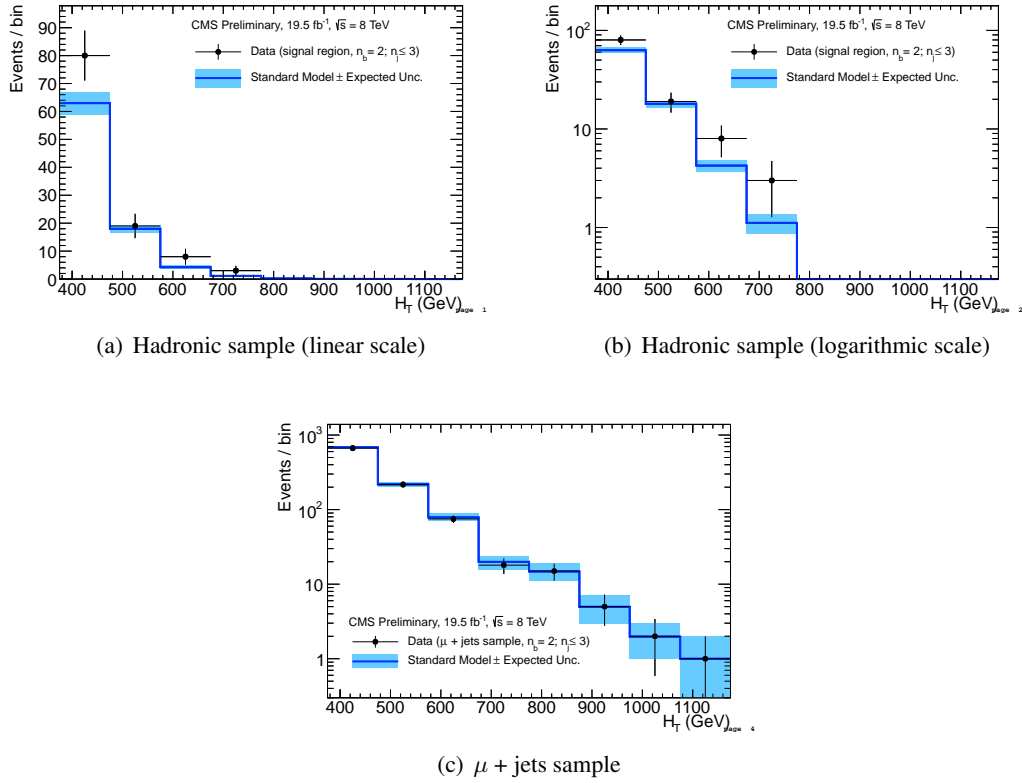


Figure 17: Comparison of the H_T -binned observed data yields and SM expectations when requiring $2 \leq n_{\text{jet}} \leq 3$ and $n_b = 2$ for the (a-b) hadronic and $\mu + \text{jets}$ samples, as determined by a simultaneous fit to both the hadronic and $\mu + \text{jets}$ data samples under the SM-only hypothesis. The observed event yields in data (black dots) and the expectations and their uncertainties (dark blue solid line with light blue bands), as determined by the simultaneous fit, are shown.

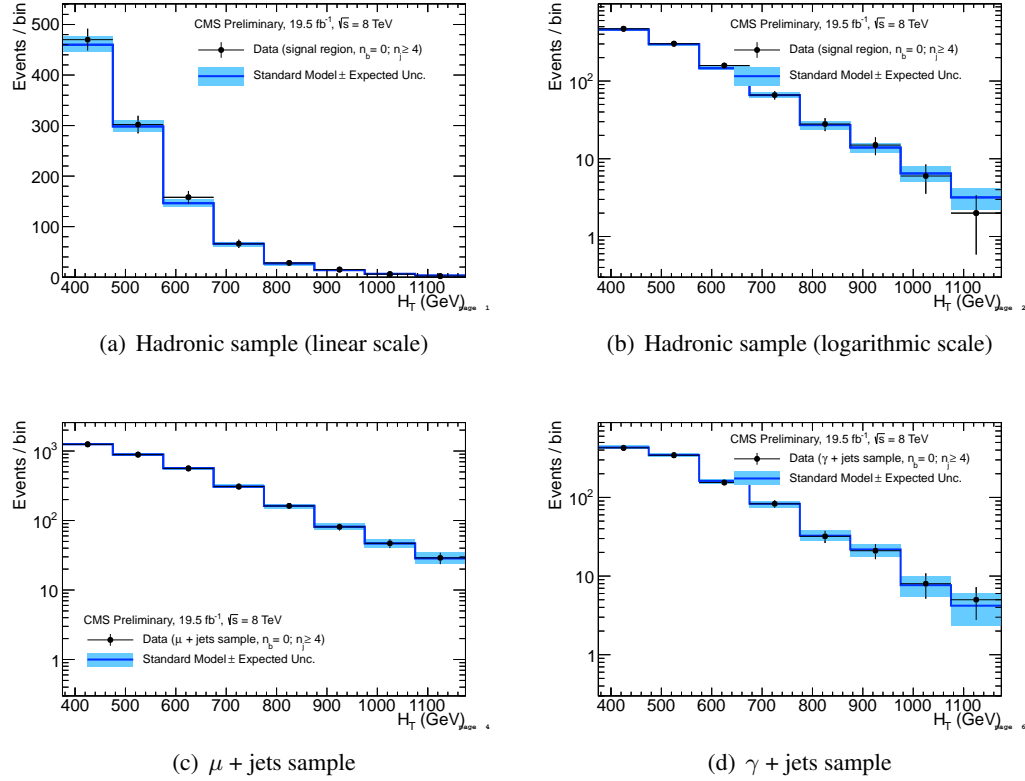


Figure 18: Comparison of the H_T -binned observed data yields and SM expectations when requiring $n_{\text{jet}} \geq 4$ and $n_b = 0$ for the (a-b) hadronic, (c) μ + jets, (d) $\mu\mu$ + jets and (e) γ + jets samples, as determined by a simultaneous fit to all data samples under the SM-only hypothesis. The observed event yields in data (black dots) and the expectations and their uncertainties (dark blue solid line with light blue bands), as determined by the simultaneous fit, are shown. For illustrative purposes only, the signal expectations (pink dashed line) for the model T2cc with $m_{\tilde{q}} = 250$ GeV and $m_{\text{LSP}} = 170$ GeV are stacked on top of the SM expectations.

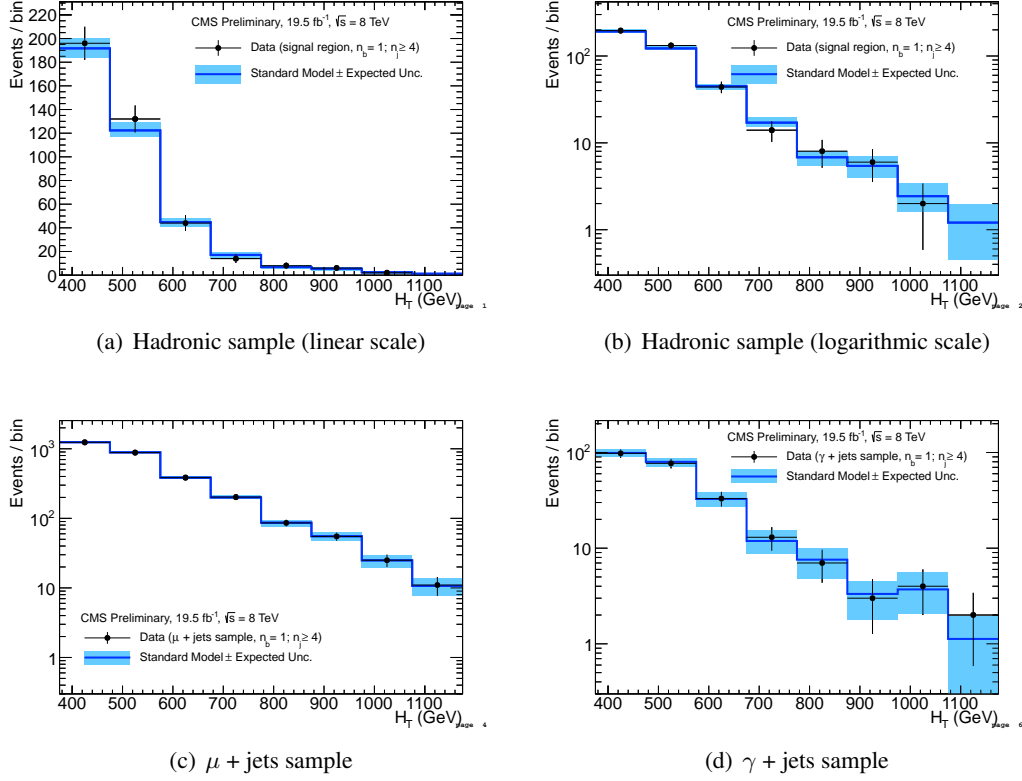


Figure 19: Comparison of the H_T -binned observed data yields and SM expectations when requiring $n_{\text{jet}} \geq 4$ and $n_b = 1$ for the (a-b) hadronic, (c) μ + jets, (d) $\mu\mu$ + jets and (e) γ + jets samples, as determined by a simultaneous fit to all data samples under the SM-only hypothesis. The observed event yields in data (black dots) and the expectations and their uncertainties (dark blue solid line with light blue bands), as determined by the simultaneous fit, are shown. For illustrative purposes only, the signal expectations (pink dashed line) for the model T2cc with $m_{\tilde{q}} = 250$ GeV and $m_{\text{LSP}} = 170$ GeV are stacked on top of the SM expectations.

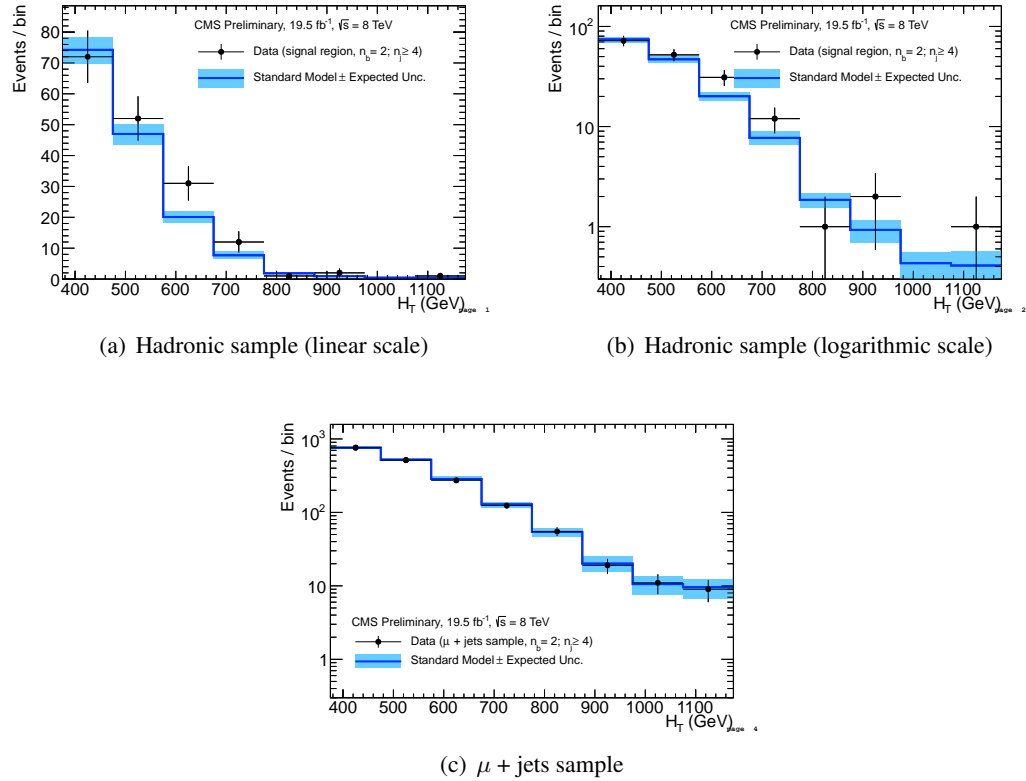


Figure 20: Comparison of the H_T -binned observed data yields and SM expectations when requiring $n_{\text{jet}} \geq 4$ and $n_b = 2$ for the (a-b) hadronic and μ + jets samples, as determined by a simultaneous fit to both the hadronic and μ + jets data samples under the SM-only hypothesis. The observed event yields in data (black dots) and the expectations and their uncertainties (dark blue solid line with light blue bands), as determined by the simultaneous fit, are shown.

A Maximum likelihood parameter values

Table 20: SM-only maximum-likelihood parameter values (0b le3j).

name	value	error
EWK^0	2.64e+03	4.7e+01
EWK^1	7.59e+02	2.2e+01
EWK^2	2.52e+02	1.1e+01
EWK^3	7.64e+01	6.0e+00
EWK^4	3.37e+01	3.5e+00
EWK^5	1.18e+01	2.0e+00
EWK^6	6.32e+00	1.4e+00
EWK^7	3.15e+00	8.9e-01
f_{Zinv}^0	0.64	0.02
f_{Zinv}^1	0.67	0.02
f_{Zinv}^2	0.70	0.02
f_{Zinv}^3	0.70	0.04
f_{Zinv}^4	0.69	0.04
f_{Zinv}^5	0.76	0.05
f_{Zinv}^6	0.76	0.06
f_{Zinv}^7	0.82	0.06
$\rho_{\mu W}^0$	1.01	0.05
$\rho_{\mu W}^1$	1.00	0.06
$\rho_{\mu W}^2$	1.00	0.07
$\rho_{\mu W}^3$	1.00	0.11
$\rho_{\mu W}^4$	1.01	0.11
$\rho_{\mu W}^5$	1.02	0.16
$\rho_{\mu W}^6$	0.98	0.15
$\rho_{\mu W}^7$	1.00	0.16
$\rho_{\gamma Z}^0$	1.02	0.04
$\rho_{\gamma Z}^1$	0.99	0.04
$\rho_{\gamma Z}^2$	1.00	0.06
$\rho_{\gamma Z}^3$	0.99	0.10
$\rho_{\gamma Z}^4$	1.02	0.11
$\rho_{\gamma Z}^5$	1.05	0.16
$\rho_{\gamma Z}^6$	0.95	0.14
$\rho_{\gamma Z}^7$	0.98	0.15

Table 21: SM-only maximum-likelihood parameter values (1b 1e3j).

name	value	error
EWK^0	4.13e+02	1.4e+01
EWK^1	1.11e+02	5.9e+00
EWK^2	3.58e+01	3.0e+00
EWK^3	1.01e+01	1.6e+00
EWK^4	3.66e+00	8.2e-01
EWK^5	1.63e+00	6.0e-01
EWK^6	4.87e-01	3.1e-01
EWK^7	1.21e-01	4.7e-02
f_{Zinv}^0	0.47	0.02
f_{Zinv}^1	0.55	0.03
f_{Zinv}^2	0.57	0.04
f_{Zinv}^3	0.64	0.07
f_{Zinv}^4	0.55	0.11
f_{Zinv}^5	0.81	0.08
f_{Zinv}^6	0.82	0.12
f_{Zinv}^7	0.00	0.83
$\rho_{\mu W}^0$	0.95	0.05
$\rho_{\mu W}^1$	0.99	0.06
$\rho_{\mu W}^2$	1.00	0.07
$\rho_{\mu W}^3$	0.98	0.11
$\rho_{\mu W}^4$	1.00	0.11
$\rho_{\mu W}^5$	1.00	0.16
$\rho_{\mu W}^6$	1.00	0.16
$\rho_{\mu W}^7$	1.00	0.16
$\rho_{\gamma Z}^0$	0.96	0.05
$\rho_{\gamma Z}^1$	0.99	0.06
$\rho_{\gamma Z}^2$	1.00	0.07
$\rho_{\gamma Z}^3$	0.96	0.11
$\rho_{\gamma Z}^4$	1.00	0.11
$\rho_{\gamma Z}^5$	0.99	0.15
$\rho_{\gamma Z}^6$	0.99	0.15
$\rho_{\gamma Z}^7$	1.00	0.16

Table 22: SM-only maximum-likelihood parameter values (2b le3j).

name	value	error
EWK^0	6.30e+01	3.8e+00
EWK^1	1.80e+01	1.5e+00
EWK^2	4.25e+00	5.4e-01
EWK^3	1.11e+00	2.7e-01
EWK^4	2.10e-01	5.9e-02
EWK^5	3.83e-02	1.8e-02
EWK^6	2.33e-02	1.7e-02
EWK^7	1.30e-03	1.3e-03
$\rho_{\mu W}^0$	0.94	0.05
$\rho_{\mu W}^1$	1.00	0.06
$\rho_{\mu W}^2$	0.98	0.07
$\rho_{\mu W}^3$	0.98	0.11
$\rho_{\mu W}^4$	1.00	0.11
$\rho_{\mu W}^5$	1.00	0.16
$\rho_{\mu W}^6$	1.00	0.16
$\rho_{\mu W}^7$	1.00	0.16

Table 23: SM-only maximum-likelihood parameter values (0b ge4j).

name	value	error
EWK^0	4.60e+02	1.6e+01
EWK^1	2.98e+02	1.2e+01
EWK^2	1.46e+02	8.2e+00
EWK^3	6.59e+01	5.7e+00
EWK^4	2.71e+01	3.3e+00
EWK^5	1.39e+01	2.2e+00
EWK^6	6.47e+00	1.5e+00
EWK^7	3.19e+00	9.5e-01
f_{Zinv}^0	0.52	0.02
f_{Zinv}^1	0.60	0.02
f_{Zinv}^2	0.61	0.03
f_{Zinv}^3	0.63	0.05
f_{Zinv}^4	0.71	0.05
f_{Zinv}^5	0.73	0.06
f_{Zinv}^6	0.74	0.07
f_{Zinv}^7	0.67	0.11
$\rho_{\mu W}^0$	0.98	0.05
$\rho_{\mu W}^1$	1.00	0.06
$\rho_{\mu W}^2$	0.97	0.07
$\rho_{\mu W}^3$	1.00	0.13
$\rho_{\mu W}^4$	1.00	0.13
$\rho_{\mu W}^5$	1.00	0.13
$\rho_{\mu W}^6$	1.00	0.13
$\rho_{\mu W}^7$	1.01	0.19
$\rho_{\gamma Z}^0$	0.98	0.05
$\rho_{\gamma Z}^1$	0.99	0.05
$\rho_{\gamma Z}^2$	0.96	0.07
$\rho_{\gamma Z}^3$	1.00	0.11
$\rho_{\gamma Z}^4$	0.99	0.12
$\rho_{\gamma Z}^5$	0.99	0.12
$\rho_{\gamma Z}^6$	1.01	0.13
$\rho_{\gamma Z}^7$	1.03	0.19

Table 24: SM-only maximum-likelihood parameter values (1b ge4j).

name	value	error
EWK^0	1.92e+02	8.5e+00
EWK^1	1.22e+02	6.1e+00
EWK^2	4.48e+01	3.5e+00
EWK^3	1.71e+01	2.1e+00
EWK^4	6.82e+00	1.3e+00
EWK^5	5.43e+00	1.5e+00
EWK^6	2.43e+00	7.9e-01
EWK^7	1.21e+00	6.3e-01
f_{Zinv}^0	0.23	0.02
f_{Zinv}^1	0.29	0.03
f_{Zinv}^2	0.38	0.05
f_{Zinv}^3	0.36	0.08
f_{Zinv}^4	0.49	0.10
f_{Zinv}^5	0.58	0.12
f_{Zinv}^6	0.70	0.11
f_{Zinv}^7	0.72	0.16
$\rho_{\mu W}^0$	0.99	0.05
$\rho_{\mu W}^1$	0.98	0.05
$\rho_{\mu W}^2$	1.00	0.07
$\rho_{\mu W}^3$	1.03	0.13
$\rho_{\mu W}^4$	0.99	0.13
$\rho_{\mu W}^5$	1.00	0.13
$\rho_{\mu W}^6$	1.00	0.13
$\rho_{\mu W}^7$	1.01	0.19
$\rho_{\gamma Z}^0$	1.00	0.06
$\rho_{\gamma Z}^1$	0.99	0.06
$\rho_{\gamma Z}^2$	1.00	0.08
$\rho_{\gamma Z}^3$	1.02	0.13
$\rho_{\gamma Z}^4$	0.99	0.13
$\rho_{\gamma Z}^5$	0.99	0.13
$\rho_{\gamma Z}^6$	1.01	0.13
$\rho_{\gamma Z}^7$	1.03	0.19

Table 25: SM-only maximum-likelihood parameter values (2b ge4j).

name	value	error
EWK^0	7.42e+01	4.4e+00
EWK^1	4.70e+01	3.1e+00
EWK^2	2.01e+01	1.8e+00
EWK^3	7.71e+00	1.1e+00
EWK^4	1.85e+00	3.4e-01
EWK^5	9.29e-01	2.3e-01
EWK^6	4.32e-01	1.4e-01
EWK^7	4.09e-01	1.5e-01
$\rho_{\mu W}^0$	1.01	0.05
$\rho_{\mu W}^1$	0.98	0.05
$\rho_{\mu W}^2$	0.94	0.07
$\rho_{\mu W}^3$	0.93	0.11
$\rho_{\mu W}^4$	1.01	0.13
$\rho_{\mu W}^5$	0.98	0.13
$\rho_{\mu W}^6$	1.01	0.13
$\rho_{\mu W}^7$	0.98	0.18

B SM-only yield tables

The following tables compare the observations in the hadronic and control samples with the maximum-likelihood expectations obtained by the SM-only fit.

Table 26: 0b 1e3j

H_T Bin (GeV)	375–475	475–575	575–675	675–775	775–875	875–975	975–1075	1075– ∞
SM hadronic	2744^{+48}_{-43}	771^{+21}_{-23}	254^{+13}_{-13}	$76.5^{+6.1}_{-4.8}$	$33.7^{+3.7}_{-3.8}$	$11.8^{+1.9}_{-2.1}$	$6.3^{+1.4}_{-1.3}$	$3.2^{+1.0}_{-0.9}$
Data hadronic	2728	766	257	77	32	9	9	4
SM μ +jets	9072^{+97}_{-113}	3543^{+56}_{-62}	1539^{+39}_{-41}	686^{+25}_{-26}	325^{+17}_{-17}	158^{+13}_{-12}	$78.6^{+7.8}_{-8.3}$	$54.1^{+7.0}_{-6.8}$
Data μ +jets	9078	3545	1538	686	326	159	78	54
SM γ +jets	3990^{+54}_{-61}	1203^{+34}_{-37}	410^{+17}_{-19}	127^{+10}_{-10}	$48.8^{+6.0}_{-6.9}$	$19.9^{+3.3}_{-4.2}$	$12.1^{+3.0}_{-2.9}$	$7.7^{+2.9}_{-2.7}$
Data γ +jets	4000	1206	408	127	50	22	10	7

Table 27: 0b ge4j

H_T Bin (GeV)	375–475	475–575	575–675	675–775	775–875	875–975	975–1075	1075– ∞
SM hadronic	456^{+15}_{-14}	291^{+12}_{-12}	148^{+8}_{-7}	$66.0^{+5.6}_{-5.2}$	$27.1^{+2.9}_{-3.4}$	$14.0^{+1.9}_{-2.1}$	$6.5^{+1.5}_{-1.2}$	$3.2^{+1.0}_{-0.9}$
Data hadronic	480	299	158	66	28	15	6	2
SM μ +jets	1260^{+36}_{-36}	891^{+29}_{-30}	566^{+23}_{-23}	308^{+20}_{-14}	162^{+11}_{-12}	$81.3^{+8.6}_{-8.1}$	$46.9^{+7.3}_{-6.1}$	$28.6^{+6.4}_{-4.4}$
Data μ +jets	1249	888	562	308	162	81	47	29
SM γ +jets	439^{+20}_{-18}	349^{+16}_{-18}	161^{+10}_{-13}	$83.0^{+7.9}_{-8.5}$	$32.6^{+5.7}_{-5.6}$	$21.8^{+3.6}_{-4.2}$	$7.7^{+2.4}_{-2.0}$	$4.2^{+1.7}_{-1.7}$
Data γ +jets	427	344	155	83	32	21	8	5

Table 28: 1b le3j

H_T Bin (GeV)	375–475	475–575	575–675	675–775	775–875	875–975	975–1075	1075– ∞
SM hadronic	426^{+15}_{-17}	114^{+6}_{-6}	$35.5^{+3.3}_{-2.8}$	$10.1^{+1.4}_{-1.5}$	$3.7^{+0.9}_{-0.8}$	$1.6^{+0.7}_{-0.6}$	$0.5^{+0.3}_{-0.4}$	$0.1^{+0.1}_{-0.0}$
Data hadronic	444	118	36	15	3	2	1	0
SM μ +jets	2282^{+50}_{-45}	789^{+26}_{-27}	325^{+20}_{-17}	139^{+11}_{-14}	$62.7^{+9.2}_{-6.5}$	$25.1^{+4.8}_{-5.1}$	$16.1^{+3.9}_{-4.1}$	$7.9^{+2.9}_{-2.9}$
Data μ +jets	2272	787	325	137	63	25	16	8
SM γ +jets	452^{+20}_{-22}	146^{+9}_{-10}	$49.3^{+6.6}_{-5.9}$	$18.1^{+3.8}_{-4.4}$	$5.6^{+2.4}_{-2.4}$	$4.3^{+1.9}_{-1.8}$	$1.4^{+1.0}_{-1.4}$	$0.0^{+0.0}_{-0.0}$
Data γ +jets	444	144	49	15	6	4	1	0

Table 29: 1b ge4j

H_T Bin (GeV)	375–475	475–575	575–675	675–775	775–875	875–975	975–1075	1075– ∞
SM hadronic	190^{+10}_{-8}	120^{+6}_{-5}	$45.6^{+3.1}_{-3.8}$	$17.1^{+2.6}_{-1.9}$	$6.8^{+1.5}_{-1.3}$	$5.4^{+1.3}_{-1.6}$	$2.4^{+0.9}_{-0.9}$	$1.2^{+0.7}_{-0.8}$
Data hadronic	206	135	45	14	8	6	2	0
SM μ +jets	1250^{+37}_{-28}	891^{+27}_{-31}	385^{+21}_{-20}	200^{+12}_{-12}	$86.6^{+9.0}_{-10.1}$	$55.3^{+7.7}_{-7.3}$	$24.9^{+4.4}_{-5.3}$	$10.7^{+3.1}_{-3.4}$
Data μ +jets	1238	881	385	202	86	55	25	11
SM γ +jets	102^{+10}_{-9}	$81.3^{+8.2}_{-7.9}$	$32.7^{+5.5}_{-5.6}$	$11.9^{+3.7}_{-3.0}$	$7.6^{+2.6}_{-2.6}$	$3.3^{+1.2}_{-1.6}$	$3.7^{+1.9}_{-1.9}$	$1.1^{+0.8}_{-1.1}$
Data γ +jets	98	77	33	13	7	3	4	2

Table 30: 2b le3j

H_T Bin (GeV)	375–475	475–575	575–675	675–775	775–875	875–975	975–1075	1075– ∞
SM hadronic	$65.0^{+4.3}_{-4.3}$	$18.4^{+1.7}_{-1.6}$	$4.2^{+0.6}_{-0.5}$	$1.1^{+0.3}_{-0.2}$	$0.2^{+0.1}_{-0.1}$	$0.0^{+0.0}_{-0.0}$	$0.0^{+0.0}_{-0.0}$	$0.0^{+0.0}_{-0.0}$
Data hadronic	78	18	8	3	0	0	0	0
SM μ +jets	681^{+26}_{-31}	217^{+14}_{-14}	$78.8^{+9.4}_{-9.3}$	$19.9^{+4.1}_{-3.8}$	$14.8^{+4.0}_{-3.9}$	$5.0^{+2.0}_{-2.1}$	$2.0^{+1.0}_{-1.0}$	$1.0^{+1.0}_{-1.0}$
Data μ +jets	668	217	75	18	15	5	2	1
Data γ +jets	36	8	4	0	0	1	0	0

Table 31: 2b ge4j

H_T Bin (GeV)	375–475	475–575	575–675	675–775	775–875	875–975	975–1075	1075– ∞
SM hadronic	$73.6^{+4.2}_{-4.2}$	$45.7^{+2.8}_{-2.9}$	$20.4^{+1.8}_{-1.8}$	$7.7^{+1.2}_{-1.0}$	$1.9^{+0.3}_{-0.3}$	$0.9^{+0.2}_{-0.2}$	$0.4^{+0.1}_{-0.1}$	$0.4^{+0.1}_{-0.2}$
Data hadronic	79	52	31	12	1	2	0	1
SM μ +jets	765^{+26}_{-27}	521^{+23}_{-22}	285^{+15}_{-17}	128^{+12}_{-10}	$54.1^{+7.5}_{-8.0}$	$20.1^{+4.6}_{-4.1}$	$10.6^{+2.9}_{-2.9}$	$9.6^{+2.9}_{-2.9}$
Data μ +jets	760	515	274	124	55	19	11	9
Data γ +jets	19	17	10	4	0	2	1	0

C Efficiencies and systematic uncertainties for simplified models

C.1 T2cc

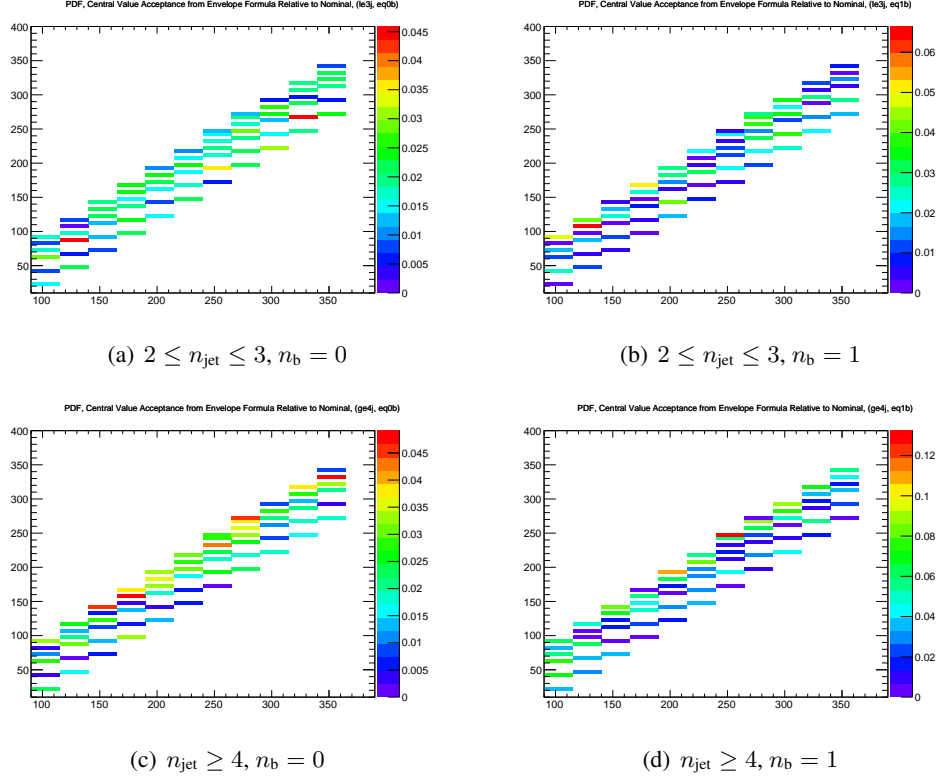


Figure 21: Ratio of efficiency times acceptance for the (middle) central value, (top) $+1\sigma$ value, (bottom) -1σ value of the envelope calculation relative to the nominal PDF set used to produce the T2cc sample.

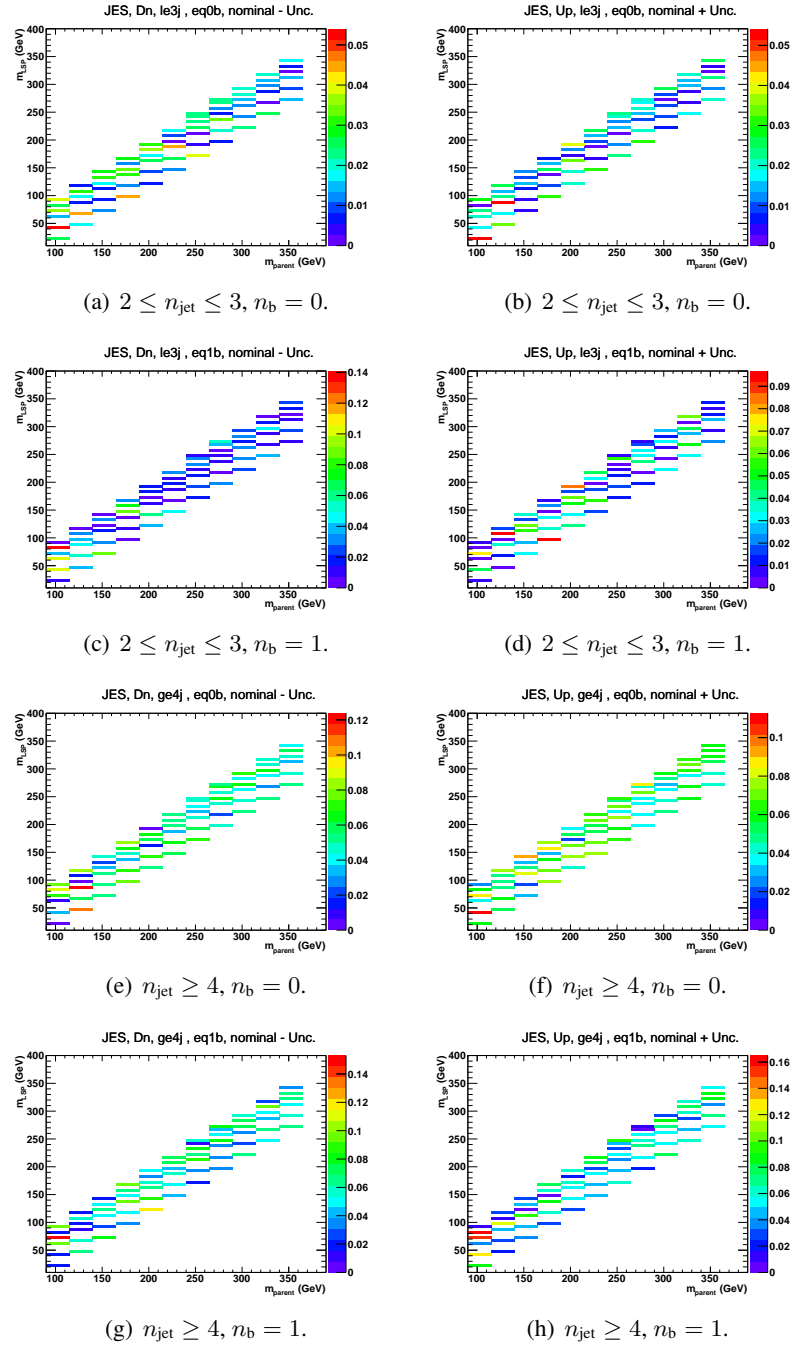


Figure 22: The fractional change in signal efficiency due to systematically (Left) increasing and (Middle) decreasing all jet energies, and (Right) the resulting (symmetric) systematic uncertainties due to JES uncertainties for T2cc.

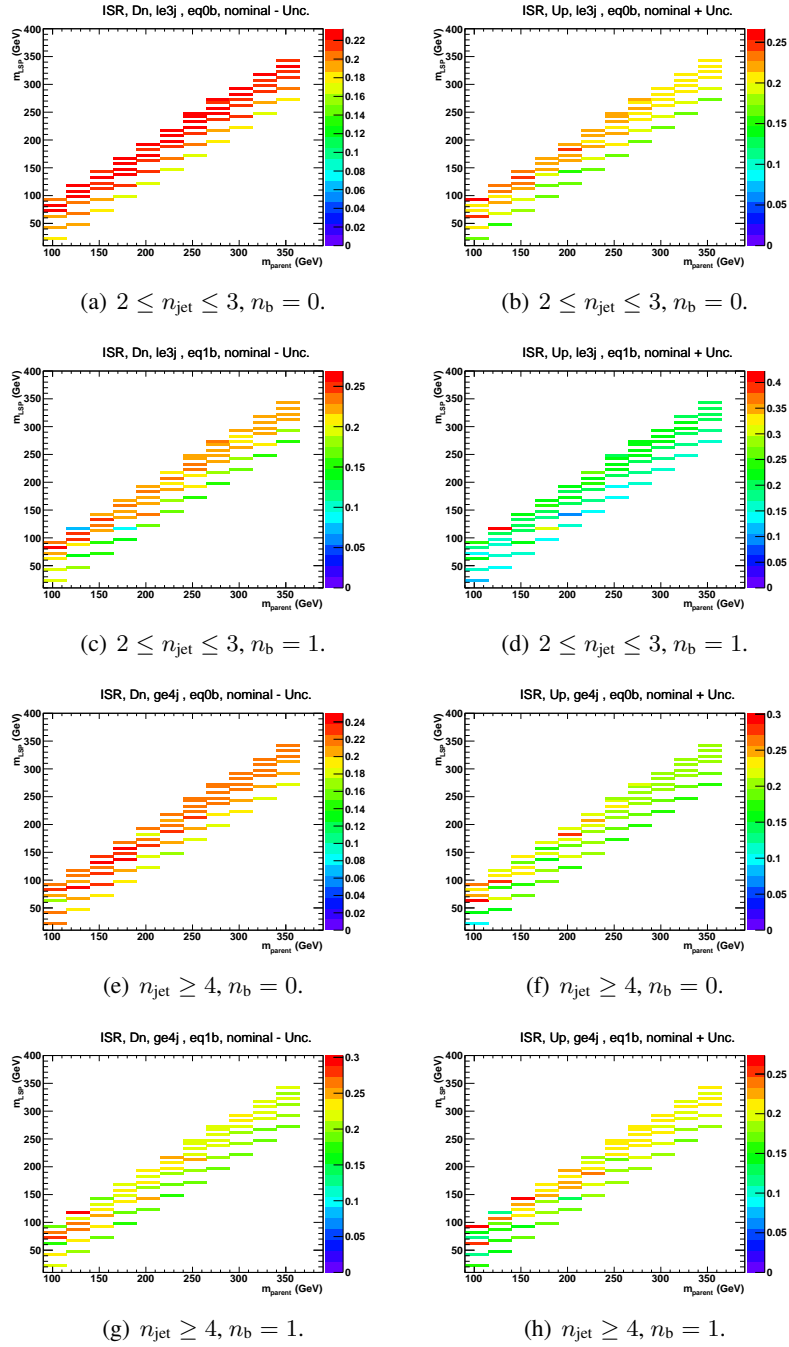


Figure 23: The fractional change in signal efficiency due to systematically (Left) increasing and (Middle) decreasing event weights according to ISR uncertainties, and (Right) the resulting (symmetric) systematic uncertainties due to ISR uncertainties for T2cc.

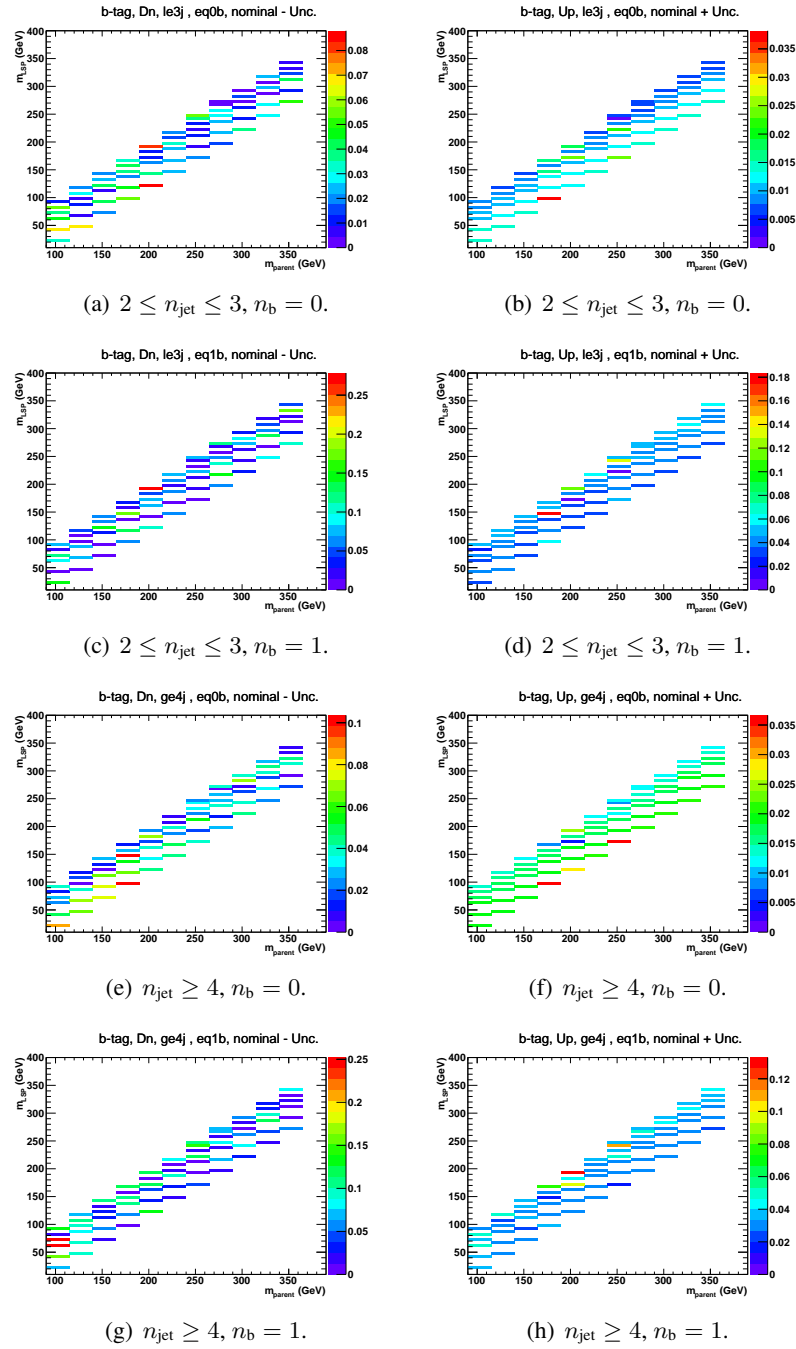


Figure 24: The fractional change in signal efficiency due to systematically (Left) increasing and (Middle) decreasing all b-tag efficiencies according to the scale factor uncertainties, and (Right) the resulting (symmetric) systematic uncertainties due to b-tag scale factor uncertainties for T2cc.

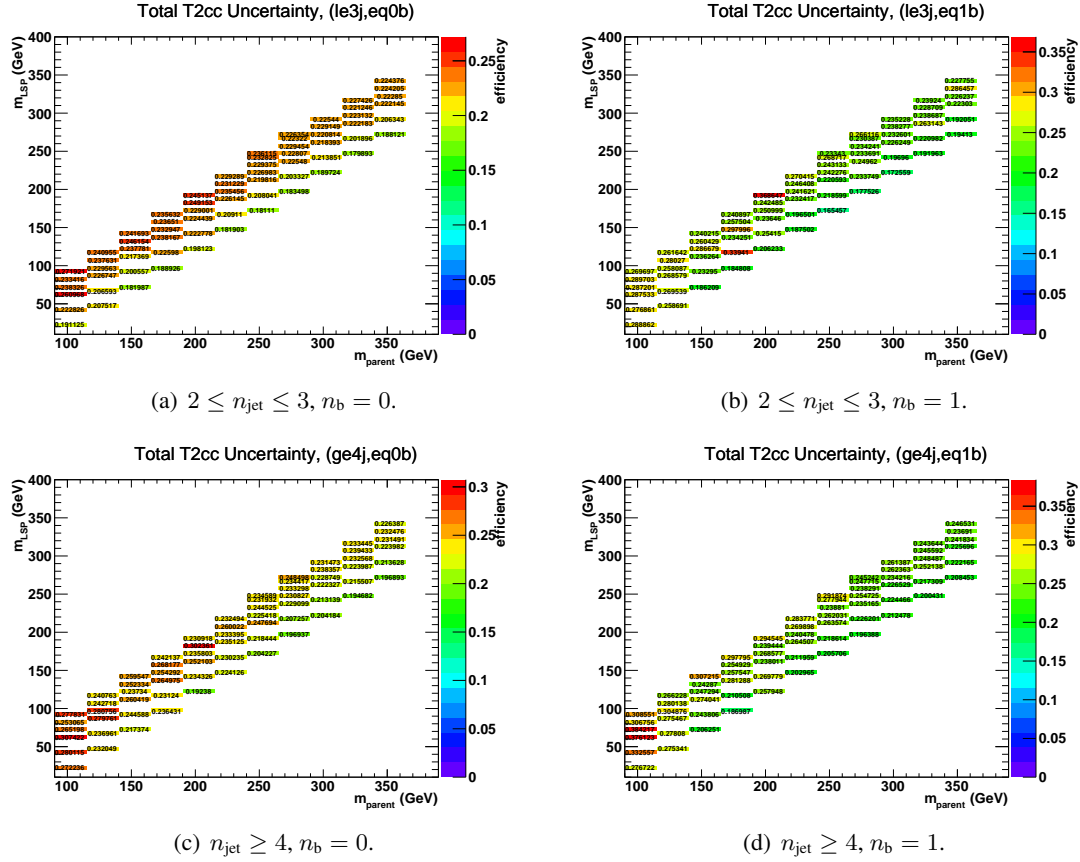


Figure 25: The total systematic uncertainty in the signal efficiency times acceptance for all relevant event categories for the T2cc interpretation.

C.2 T2tt

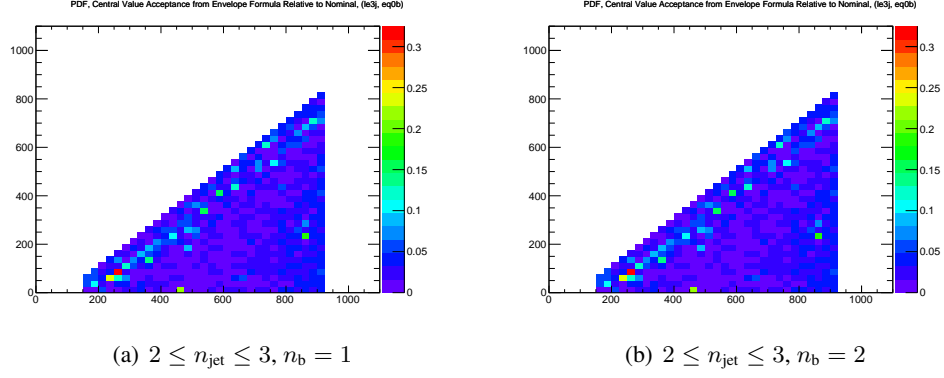


Figure 26: Ratio of efficiency times acceptance for the (middle) central value, (top) $+1\sigma$ value, (bottom) -1σ value of the envelope calculation relative to the nominal PDF set used to produce the T2tt sample.

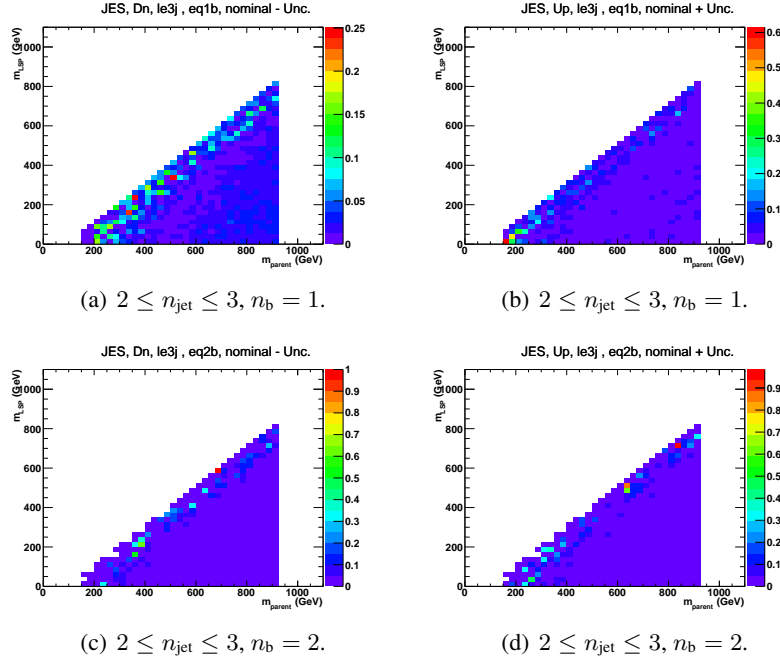


Figure 27: The fractional change in signal efficiency due to systematically (Left) increasing and (Middle) decreasing all jet energies, and (Right) the resulting (symmetric) systematic uncertainties due to JES uncertainties for T2tt.

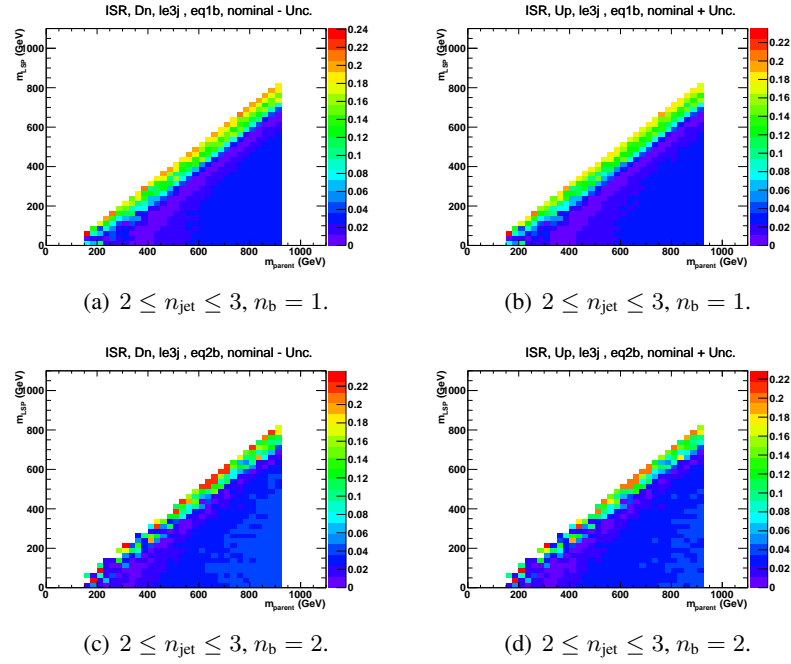


Figure 28: The fractional change in signal efficiency due to systematically (Left) increasing and (Middle) decreasing event weights according to ISR uncertainties, and (Right) the resulting (symmetric) systematic uncertainties due to ISR uncertainties for T2tt.

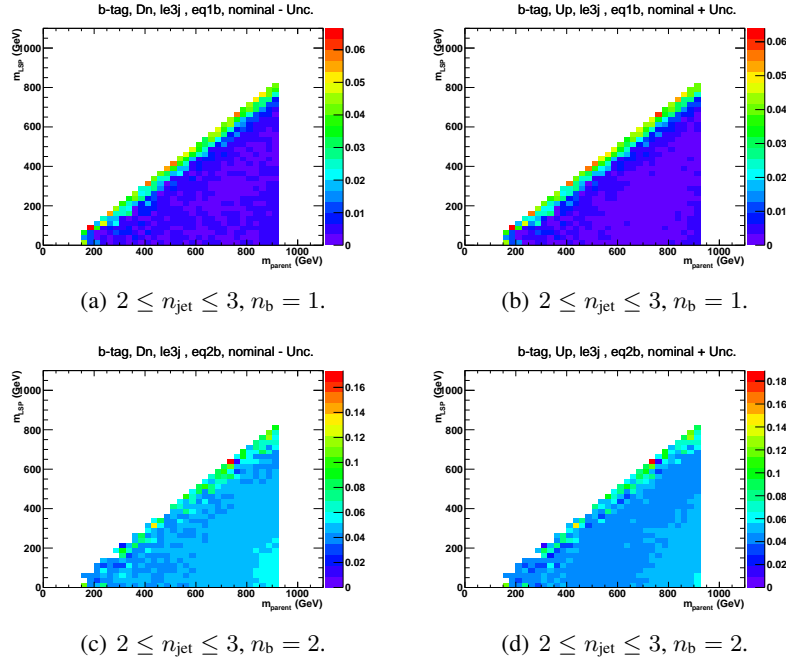


Figure 29: The fractional change in signal efficiency due to systematically (Left) increasing and (Middle) decreasing all b-tag efficiencies according to the scale factor uncertainties, and (Right) the resulting (symmetric) systematic uncertainties due to b-tag scale factor uncertainties for T2tt.

References

- [1] G. Cowan et al. Asymptotic formulae for likelihood-based tests of new physics. *Eur. Phys. J. C*, 71:1554, 2011.
- [2] T Junk. Confidence level computation for combining searches with small statistics. *Nucl. Instr. and Meth. A*, 434:435, 1999.
- [3] Edward M. Laird. *A Search for Squarks and Gluinos with the CMS Detector*. PhD thesis, Princeton University, 2011.
- [4] Lorenzo Moneta, Kevin Belasco, Kyle Cranmer, Alfio Lazzaro, Danilo Piparo, Gregory Schott, Wouter Verkerke, Matthias Wolf, Kevin Belasco, Kyle Cranmer, Alfio Lazzaro, Danilo Piparo, Gregory Schott, Wouter Verkerke, and Matthias Wolf. The RooStats Project. *PoS, ACAT2010(arXiv:1009.1003):057*, Sep 2010. Comments: 11 pages, 3 figures, ACAT2010 Conference Proceedings.
- [5] A. L. Read. Presentation of search results: the cl_s technique. *J. Phys. G*, 28:2693, 2002.